# Grazing, skipping and sliding: analysis of the non-smooth dynamics of the DC/DC buck converter

Mario di Bernardo †, Chris Budd ‡ and Alan Champneys †

† Department of Engineering Mathematics,
University of Bristol, Bristol BS8 1TR, U.K.
‡School of Mathematical Sciences, University of Bath, Bath BA2 7AY, U.K.

**Abstract.** In this paper, we provide an analytical insight into the observed nonlinear behaviour of the buck converter and link this with the study of a wider class of piecewise-smooth systems. After introducing the buck converter model and background, we describe the most fascinating features of its dynamical behaviour. We then introduce the so-called grazing and sliding solutions and discuss their role in determining many of the buck converter's dynamical oddities. In particular, a local map is studied which explains how the grazing bifurcations cause sharp turning points in the bifurcation diagram of periodic orbits. Moreover, we show how these orbits accumulate onto a sliding trajectory through a "spiralling" *impact adding* scenario. The structure of such a diagram is derived analytically and is shown to be closely related to the analysis of homoclinic bifurcations. The results are shown to match perfectly with numerical simulations. The sudden jump to large-scale chaos and the fingered structure of the resulting attractor are also explained.

Short title: Non-smooth dynamics of the DC/DC buck converter

September 22, 1997

## 1. Introduction

In recent years, much research effort has been spent in investigating the dynamics of so-called DC/DC *buck* converters used in power electronics. These systems are used whenever there is the need for adjusting a given DC voltage to a lower value. Mathematically, they can be described by piecewise smooth systems of ODEs, switching between two different linear systems whenever a linear combination of the system states crosses an appropriately given periodic piecewise-linear reference signal.

Nonlinear phenomena including bifurcation and chaos have been found in the buck and related converters both numerically and experimentally by a number of authors [6, 3, 17, 16, 18, 21, 2, 7, 19]. For example, it has been shown that by varying the external forcing voltage, the fundamental periodic solution (the desired state in most applications) undergoes an initial period doubling cascade. At higher forcing voltages, the usual period-doubling route is interrupted by an abrupt enlargement of the resulting *small scale* chaotic attractor. The system then starts to evolve along a *large scale* chaotic attractor occupying approximately *five zones* in phase space. Periodic and chaotic attractors have also been discovered at lower input voltages, coexisting with the fundamental state, albeit with small basins of attraction [6]. Recent simulations by the first author and co-workers [6], have focussed on such a *three-zone* chaotic attractor. Within this parameter region, a family of three-periodic orbits characterised by differing numbers of switchings per period, was found to be organised along a *spiralling bifurcation diagram*. Numerical evidence presented below shows that a similar spiral structure underlies the larger five-zone chaotic region also.

Other recent work by the first author and co-workers [8] has conducted an analytical investigation of some the simplest periodic orbits in the buck converter by analysing an appropriate *switching map*. This mapping describes the circuit dynamics from one switching instant to the next, and is closely analogous to mappings used in the study of other piecewise smooth systems such as impact oscillators [1, 11, 10]. Using this approach, conditions for infinite local stretching in the dynamics were derived and the first period-doubling bifurcation accurately detected. However, at present, almost all of the dynamical oddities mentioned above remain unexplained.

The main aim of this paper is to give an analytical explanation of the unexplained phenomena in the buck converter dynamics, for instance the sudden enlargement to a five-zone chaotic attractor. We also seek to uncover features of the dynamics in the large-scale chaotic region that may apply to wider classes of system. Our major achievement is to describe the structure of the observed spiralling bifurcation diagrams by analysing a nearby co-dimension-two periodic solution, a so called *sliding* trajectory. Such a trajectory remains for finite time within the discontinuity set of the differential equations [9]. It will turn out that the unfolding of sliding leads naturally to spiral bifurcation diagrams, and has a close analogy with the analysis of Shil'nikov homoclinic bifurcations (see [14], for example). It will be shown that the limbs of the spiral have sharp turning points, caused by so-called *grazing* bifurcations, i.e. when the linear combination of the two system states passes through the corner of the periodic reference signal.

Since the original preparation of this paper we have become aware of the independent related work by Yuan *et al.* [20] on border-collision bifurcations in a different buck converter configuration. Their work, which is largely numerical, puts grazing bifurcations in DC/DC converters within the general framework of so-called border-collision bifurcations occuring in arbitrary piecewise-smooth systems. In their

example, the enlargement jump occurs before the accumulation of period-doublings and is directly attributable to a grazing (border collision) bifurcation. In contrast, in our results grazing plays a more subsidiary role, and the main focus of the present paper is on an unfolding of sliding.

The rest of the paper is outlined as follows. After introducing the buck converter model in §2, we will briefly review the main features of its dynamical behaviour in §3. In so doing we will introduce more carefully the concepts of grazing and sliding in the present context. In §4 a local map will be derived which explains how grazing causes sharp turning points in the bifurcation diagram of periodic orbits. §5 then contains the main results of the paper on an unfolding of sliding solutions, showing via explicit construction of solutions near sliding how a spiral bifurcation diagram arises. §6 will address the sudden jump to large scale chaos and the structure of the resulting chaotic attractor. Finally, §7 will draw conclusions and outline extensions of the theory to a wider class of piece-wise smooth systems.

## 2. The DC/DC buck converter

An elementary buck converter can be implemented in a circuit as represented in Fig. 1. This consists of a basic $RLC$ circuit, a diode and a switching element. The aim of the circuit is to maintain a desired voltage, lower than that provided by the input battery $E$, across the load resistance $R$. This can be achieved by appropriately turning on and off the switch $S$, so that the circuit is repeatedly forced by the external forcing voltage source $E$. The switching action is usually implemented through a Pulse

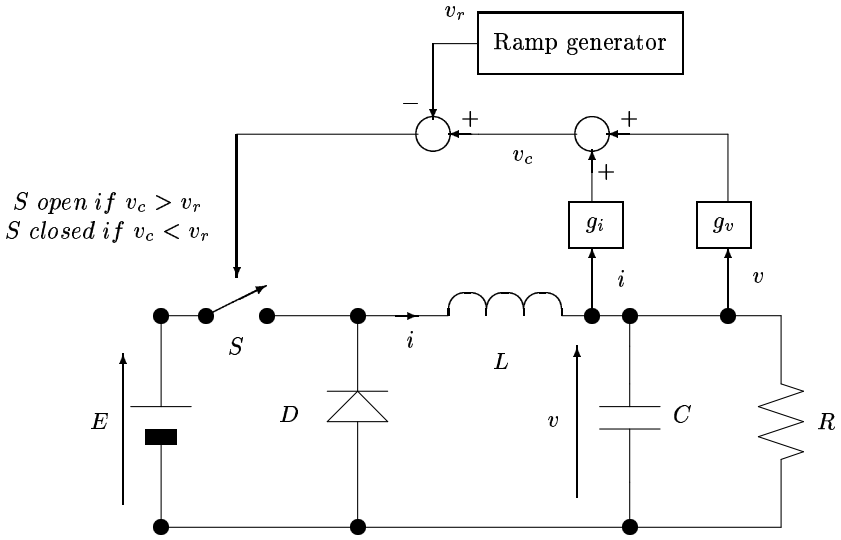


**Figure 1.** The DC/DC buck converter.

Width Modulated (PWM) feedback law. Namely a linear combination of the two system states, $v_c(t) = g_1 i(t) + g_2 v(t)$ (in the present work $g_1 = 1, g_2 = 0$), is compared with a given asymmetric sawtooth (ramp) signal of assigned period $T$ as shown in fig. 2. The circuit switch, $S$, is then turned on whenever the ramp signal becomes

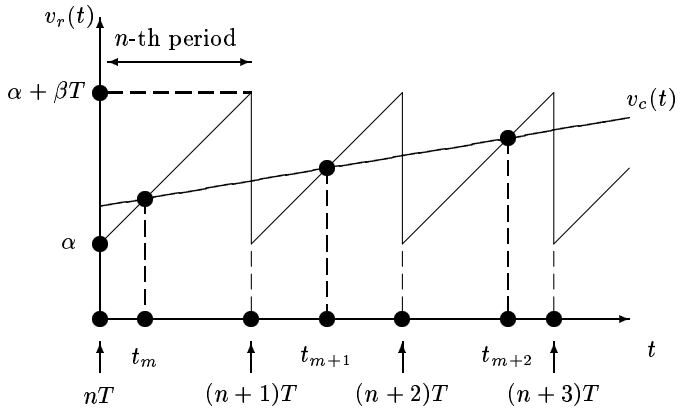


**Figure 2.** Standard DC/DC converter PWM operating conditions: one impact per period.

greater than the combination of the two states and turned off when the ramp signal falls below this combination. Hence, a switching occurs whenever $v_c(t)$ crosses the ramp (either within the ramp period or at $t = nT,\ n = 1, 2, ...$).

### *2.1. System Modelling*

Whether the switch is on or off, the buck converter can always be described as a second order linear system, whose states are the voltage $v$ across the capacitor, and the current $i$ along the inductor. The equations take the form

$$\begin{aligned} \frac{dv}{dt} &= -v/RC + i/C, \\ \frac{di}{dt} &= -v/L + \begin{cases} 0 & \text{if} \quad v > v_r(t) = \gamma + \eta(t \bmod T) \quad \text{(OFF)} \\ E/L & \text{if} \quad v < v_r(t) = \gamma + \eta(t \bmod T) \quad \text{(ON)}. \end{cases} \end{aligned} \tag{1}$$

Equation (1) is only one possibility among a class of buck converters, modelled by ODEs of the form

$$\dot{y} = \begin{cases} A_1 y + B_1 u, & \text{if } g_1 y_1 + g_2 y_2 < v_r(t), \\ A_2 y + B_2 u, & \text{if } g_1 y_1 + g_2 y_2 > v_r(t), \end{cases} \tag{2}$$

where in our case $y = (y_1 \quad y_2)^T = (v, i)^T$ and:

$$\begin{aligned} A_1 &= A2 = \begin{pmatrix} 0 & -1/L \\ 1/C & -1/(RC) \end{pmatrix}, \\ B_1 &= \begin{pmatrix} 1/L \\ 0 \end{pmatrix}, \qquad B_2 = \begin{pmatrix} 0 \\ 0 \end{pmatrix} \\ g_1 &= 1, \qquad g_2 = 0, \\ u(t) &= E, \qquad v_r(t) = \gamma + \eta(t \bmod T); \end{aligned}$$

It is relevant to point out that although we will consider the case of voltage-controlled converters ($g_1 = 1, g_2 = 0$ in (2)), the results described in these paper can be easily generalised to any other control strategy ($g_1, g_2 \in \mathcal{R}$).

For the remainder of this paper we take the parameter values motivated by the experimental literature [3]. In particular:

$$\begin{array}{lll} L = 20 \text{ mH}, & C = 47\mu\text{F}, & R = 22\ \Omega, \\ T = 400\ \mu\text{sec}, & \gamma = 11.75238095 \text{ V}, & \eta = 1309.523810 \text{ V/sec}, \end{array} \tag{3}$$

and $E \in (15, 40)V$.

### *2.2. Definitions*

Looking at the converter equations, we will say that the system is in the OFF phase when the capacitor voltage is larger than the ramp signal, $v(t) > v_r(t)$, and in the ON phase if $v(t) < v_r(t)$.

Among the switchings, we will define *Asynchronous–switching* (or $A$-switching) as switching taking place within a ramp cycle, and *$T$–switching* as one occurring at multiples $nT$ of the ramp period $T$. In what follows we shall label solutions of (1) by pairs of integers $(m, n)$, where $n$ indicates the number of $T$-switchings and $m$ the number of $A$-switchings. Occasionally, by analogy with impact oscillators we shall refer to $A$-switchings as *impacts* and $T$-switchings as *stroboscopic points*.

During standard operating conditions, the system evolves along a $T$-periodic solution characterised by one $A$-switching per period, i.e. one $A$-switching and one $T$-switching occurring during each cycle of the ramp signal. In addition to this, the following other situations are possible (see Fig. 3):

- more than one switching occurs during the one period of the modulating ramp signal (*multiple pulsing*);
- the system evolves along a generic $nT$-periodic orbit, characterised by $m$ $A$-switchings per period. We will refer to such a solution as a ($\mathcal{P}(m, n)$ *orbit*) ;
- the voltage misses one or more T–switchings (*skipping* phenomenon), $v(nT) > v_r(nT)$;
- the voltage grazes the reference ramp signal at time instants multiples of $T$ (*grazing*), $v(nT) = v_r(nT)$. In particular, we will say *external* a grazing occurring from outside the ramp, while *internal* that taking place from the inside.
- an infinite number of impacts occurs within the same period of the ramp (*sliding*); notice that periodic *sliding* trajectories are also possible;

Notice that, as reported in [8, 12], the buck converter dynamics can be studied by using two different types of discrete maps. The former, called a *stroboscopic map*, is defined as the mapping of the two system states, $(v(t), i(t))$, from one $T$-switching to the next:

$$(v_n, i_n) \mapsto (v_{n+1}, i_{n+1})$$

The latter, which takes the name of *impact map*, is instead defined as the mapping from the pair consisting of an $A$-switching instant, $\tau_m$, and the corresponding system current, $i_m = i(\tau_m)$, to the next:

$$(\tau_m, i_m) \mapsto (\tau_{m+1}, i_{m+1})$$

As reported in [8], by using the impact map it is possible to give conditions for *infinite local stretching* of the phase space. This occurs when the voltage derivative is equal

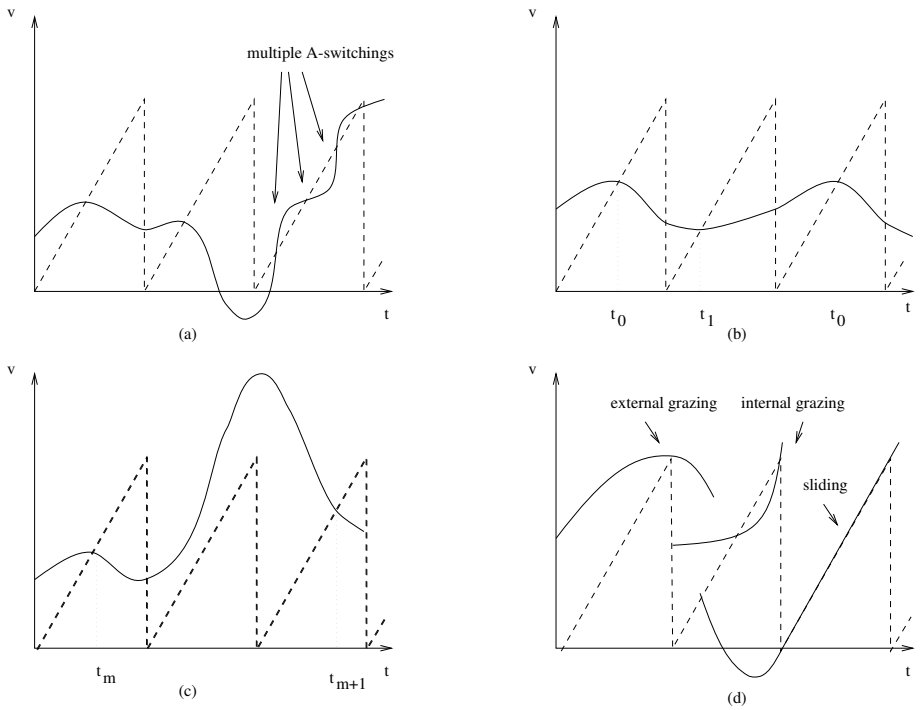


**Figure 3.** Possible behaviour: (a) multiple $A$-switchings, (b) $P(2,2)$ orbit (it repeats itself after two A-switchings), (c) an orbit which skips , (d) possible grazing and sliding.

to that of the ramp at a $T$-switching, i.e. $\dot{v}(t) = \dot{v}_r(t)$. (See [8, 6, 5] for a discussion and also for analytical derivation of both maps and their use in locating analytically period-doubling bifurcations and necessary conditions of existence for a given periodic orbit.)

## 3. Overview of the buck converter's underlying dynamics

The dynamics of (1) have been described in some detail in the literature, both numerically and experimentally [3, 4, 8, 12, 6, 5, 16, 21, 2]. In this section we summarise this work, focussing on the results by the first author and co-workers in [6, 5]. We will present in the process some new more detailed numerical results.

The overall bifurcation diagram of output voltage $v(t)$ against input voltage $E$ is shown in Figs. 4, 5. These were obtained numerically by simulating the converter evolution over 5000 ramp cycles for each value of the input voltage $E$, starting from a spread of initial conditions, $(v_0, i_0) \in [11.4, 12.8] \times [0.4, 0.8]$. After a transient of 3000 ramp cycles, the value of the voltage at each $T$-switching and $A$-switching were stored and only last 100 stroboscopic and $A$-switching points plotted in fig. 4 and fig. 5 respectively.

For sufficiently small $E$, the only recurrent behaviour observed is a stable $P(1,1)$ orbit. As the input voltage is increased through $E = 24.516$ this periodic orbit undergoes a period-doubling cascade which accumulates into (small scale) chaos. However, the usual sequence for uni-modal maps is suddenly interrupted by an abrupt

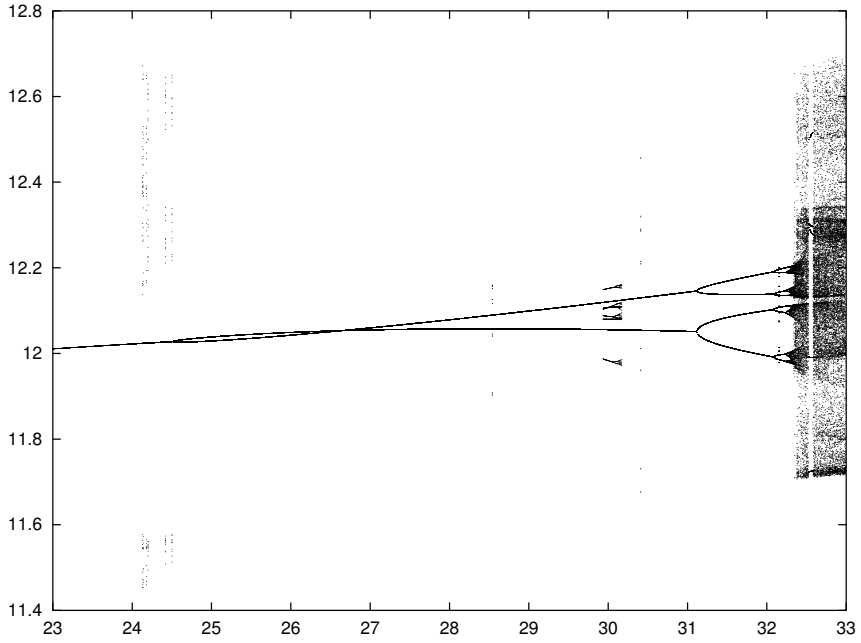


**Figure 4.** Buck converter bifurcation diagram of $v$ against $E$ in the stroboscopic Poincaré section (after [6]) showing competing attractors, a period doubling route to chaos and the sudden enlargement around $E = 32.34$

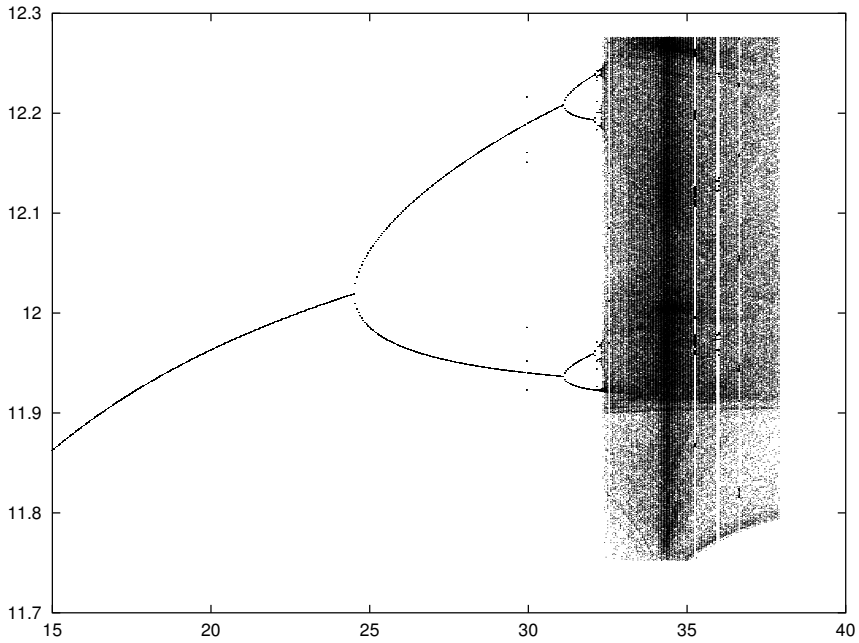


**Figure 5.** Buck converter bifurcation diagram for $v$ sampled at $A$-switching points (after [5]) over a longer $E$-range that the previous figure. Note that the period-doublings appear quadratic in this projection and note the fine structure of the large-scale chaotic region for $E > 32.34$

enlargement of the resulting *small scale* chaotic attractor for $E \approx 32.342V$. At various windows of $E$-values less than the jump, several 3, 6 and 12-period periodic and chaotic attractors with small basins of attractions are observed to coexist with the fundamental dynamics (they appear like points introduced by a bad photocopier in Fig. 4 !); see [6] for more details.

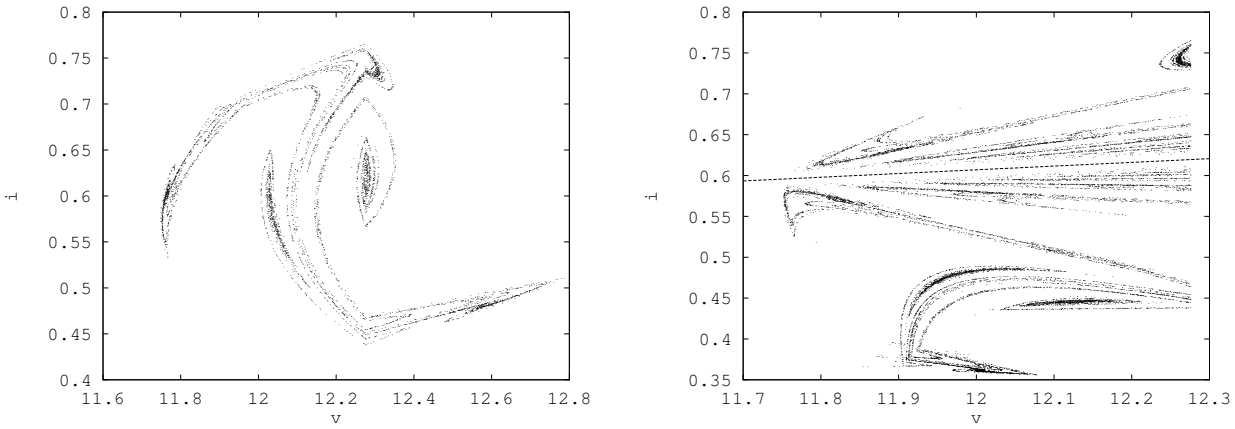


**Figure 6.** Large scale chaotic attractor for $E = 35V$: (a) at $T$-switching points; (b) at $A$-switching points, the dashed line represents the sliding line corresponding to trajectories being tangent to the ramp $v_r(t)$.

For $E > 32.342$ *large scale* chaos is then observed and the converter starts evolving along the chaotic attractor depicted in Fig. 6. Notice the curious structure of this broad band attractor. When viewed at stroboscopic points, the attractor has a five zone topology (see the five dark zones in Fig. 6(a), and [12] for more details). Moreover, when viewed at $A$-switching points (fig. 6(b)) we note that the attractor has a fingered structure and is characterised by consistent stretching in the Poincaré plain. Plotting graphs of solutions, fig. 7, reveals that this fingering is associated with multiple $A$-switchings occuring in one of the five periods owing to the trajectory being close to sliding (see §6 below for more details).

It is worthwhile to note that, aside from the small-basin-of-attraction 3, 6, 12-periodic windows, the observed dynamics (including period-doubling and chaos) for $E < 32.342$ is all of type $(1, \cdot)$, that is one $A$-switching per period. The sudden enlargement can best be characterised by the point at which the average number of $A$-switchings per period on the observed attractor first goes above 1 (see Fig. 8). Note that this quantity reaches a peak at around $E = 34.34$. This coincides with the parameter value at which we can compute a 5-periodic orbit which (appears) to slide, that is become tangent to the ramp (fig. 7(d)). In a formal sense, this trajectory may be labelled $P(\infty, 5)$, and numerically we can find nearby $P(m, 5)$ orbits for $m$ apparently arbitrarily large. Fig. 7 depicts two such periodic solutions. Numerically tracing such solutions as a parameter varies has proved a cumbersome task. Because of the non-smoothness of (1), standard continuation codes such as AUTO were not found to cope. Instead we have combined a simple numerical shooting algorithm based on a variable step-size, variable order Adams method (NAG routine `d02cbf`) allied with the the robust nonlinear solver SNSQE [15]. Fig. 9 shows some preliminary calculations suggesting that these five-periodic orbits lie in an approximate double

spiral accumulating on the spiralling trajectory. Note the corners in the bifurcation diagram, which are caused by grazing bifurcations.

A similar structure of periodic orbits appears in a detailed numerical investigation [6] of the three-zone chaotic attractor co-existing with the main bifurcation branch for $E \in (24, 24.5)$, see Fig. 4. The existence of a whole family of three-periodic orbits, coexisting with the chaotic regime, was outlined. These solutions were shown to be organised along a spiral bifurcation diagram, reproduced here as Figs. 9, 10. In [6], though, this structure is left unexplained.

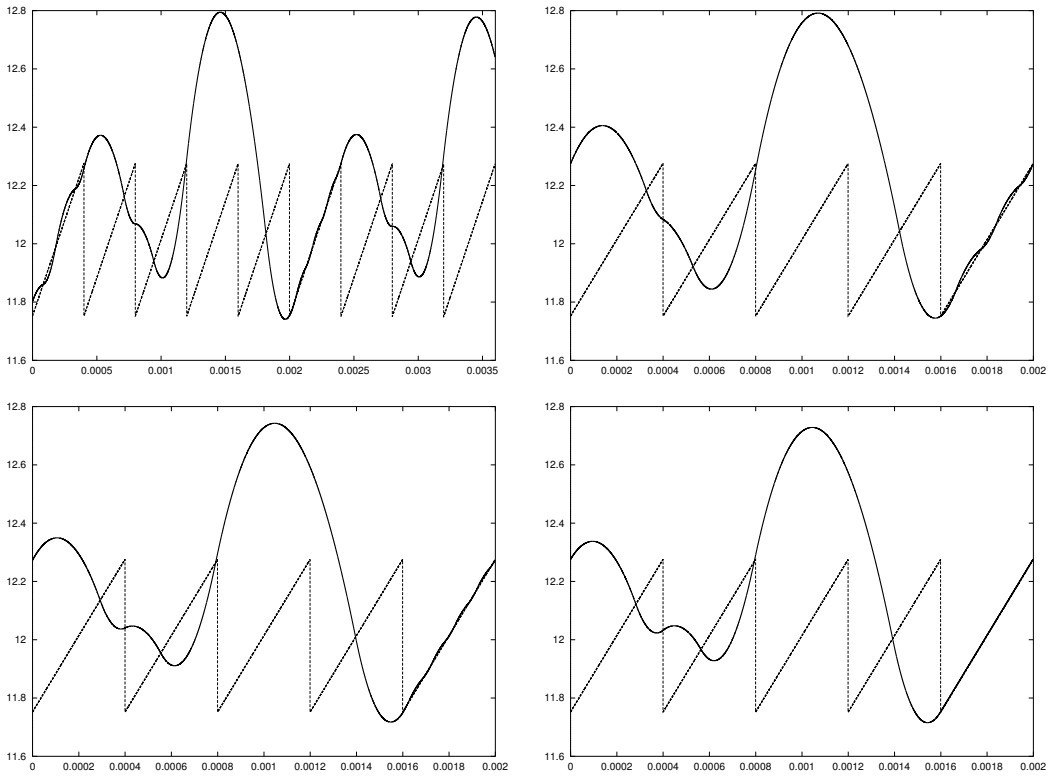

**Figure 7.** Trajectories plotted as graphs of $v(t)$ for $E = 34.33998$ (a) A chaotic solution, (b) $P(5,5)$ and (c) $P(10,5)$ periodic solutions (d) A (near) sliding periodic trajectory

In what follows we will try to explain analytically the structure of the spiralling bifurcation diagram. The key shall be a local analysis of the sliding trajectory apparently observed for $E = 34.33998$. However, the analysis in §5 shows that periodic sliding trajectories are of co-dimension-two for systems of the form (2) and further more detailed numerics shows that the trajectory in fig. 7 is not quite $P(\infty, 5)$ but is $P(m, 5)$ for $m$ large. This strongly suggests that (1) is sufficiently close to the co-dimension-two point to enable explanation of its dynamics in terms of a local analysis a sliding periodic orbit. It is such an analysis that forms the main content of §5. §6 then turns to a partial explanation, using the same theory, of the fingered structure of the five-zone strange attractor. First, though, we turn our attention to an unfolding of grazing bifurcations.

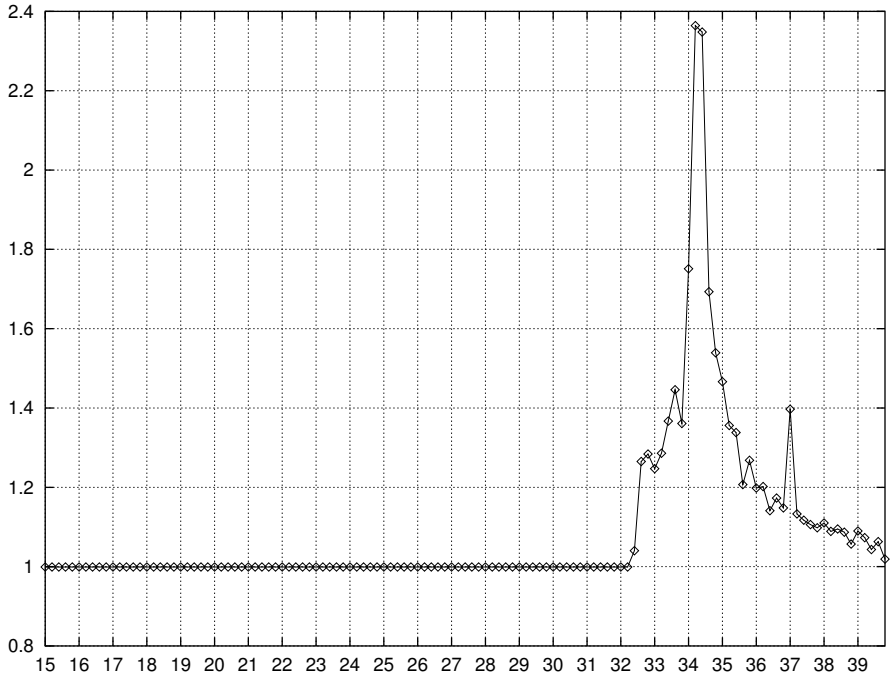


**Figure 8.** Average number of $A$-switchings-per-period on the attractor, against $E$

## 4. Local analysis of grazing

Fig. 10 shows the bifurcation diagram of the $O(\cdot, 3)$, as reported in [6]. It is clear that a grazing with the top of the ramp in the third period is taking place at each corner (black spots in fig. 10,11. The other possibility, a grazing at the bottom corner of the ramp is not observed. So we restrict our attention here to bifurcations where a periodic solution gains an extra switching (impact) in its last period, due to a grazing with the top. We seek to demonstrate that this necessarily causes its bifurcation diagram to exhibit a sharp turning point or *corner*. A similar phenomenon characterises the spiral of 5-periodic orbits depicted in fig. 9.

In what follows we will consider the case of two five periodic orbits characterised by an external and internal grazing respectively. These orbits are located at the corners of the spiral shown in fig. 9. Namely, the periodic orbit characterised by an external grazing point is the one located at $E = 32.789985, i_0 = 0.599551$ while the one containing an internal grazing is located at $E = 53.500001, i_0 = 0.738109$. Notice that in both case $v_0$ is fixed at the top of the ramp, hence $v_0 = 12.276190$.

By perturbing the system in a neighbourhood of these grazing trajectories it can be observed that the local voltage map remains locally linear, while the current one is characterised by a sharp corner. This is the case for both the *internal* and *external* grazing phenomena, as shown in figs. 12 and 13 respectively. Here, a small perturbation $\delta$ is applied to the system initial condition and the voltage and current in a neighbourhood of the grazing values are plotted.

In seeking to analyse such maps, we shall consider two simplified mappings which capture the qualitative features observed in Figs. 12 and 13. The results obtained are equally valid for both the internal and external grazing, the two cases simply leading

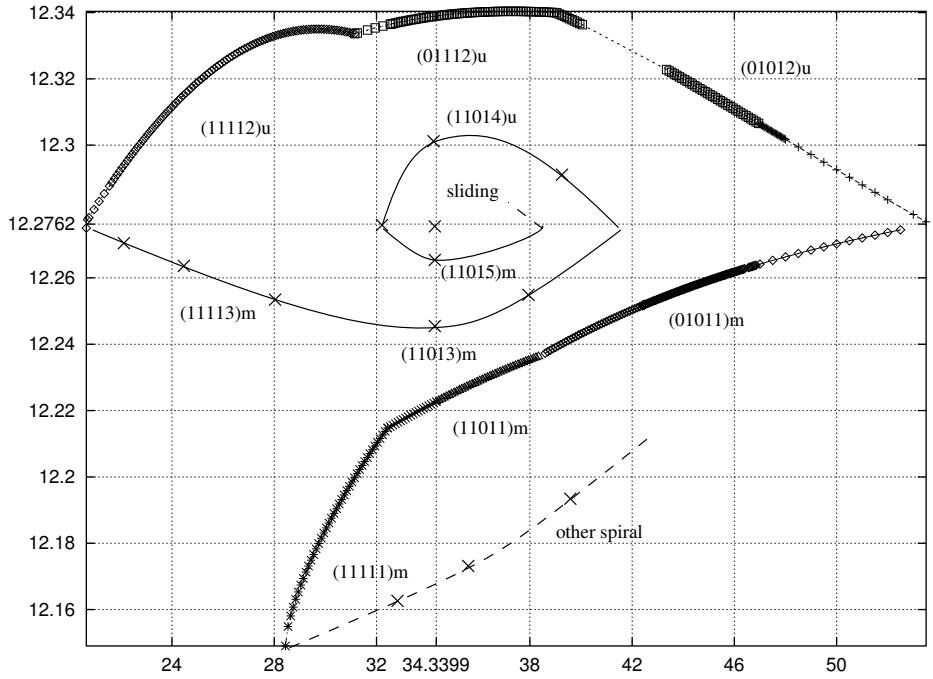


**Figure 9.** Numerical continuation of 5-periodic orbits, showing preliminary evidence for a spiralling bifurcation diagram. Orbits of different types are tagged with the number of impacts occurring in each of the five periods and the letter $m$ or $u$ according to whether the initial conditions are above or below the end-of-the-ramp line ($v \approx 12.27V$) respectively. Points indicated by crosses, squares and diamonds are exact numerical results whereas lines represent conjectured interpolations.

to different signs of the coefficients of the maps derived below. We introduce two local coordinate systems $(x_1, y_1)$, $(x_2, y_2)$ so that the $x$-coordinate and $y$-coordinate are related to the system voltage and current respectively. On the basis of the numerical evidence, it is then possible to construct two appropriate Poincaré local maps which at a critical parameter value $\mu = 0$ have a fixed point of their composition, see Fig. 14.

We construct two Poincaré sections $\Pi_1$ and $\Pi_2$ as depicted in fig. 14 and consider the two maps

$$\Sigma_1 : \Pi_1 \mapsto \Pi_2, \quad \Sigma_2 : \Pi_2 \mapsto \Pi_1. \tag{4}$$

Now, we assume that we are considering a small enough perturbation of the grazing trajectory in both phase and parameter space such that all trajectories governed by $\Sigma_2$ have the same number of $A$-switching in the same order. In such a circumstance, $\Sigma_2$ must be smooth and all the piecewise linear behaviour is contained in the map $\Sigma_1$. Hence we can take $\Sigma_2$ to be a locally linear map (under a non degeneracy assumption). Now we have some freedom in the choice of local co-ordinates $(x_1, y_1)$ and $(x_2, y_2)$ and thus we are free to choose $\Sigma_2$ to be the identity. (Alternatively we may consider that $\Sigma_1$ to be the map from time instantaneously after $pT$, the time instant of the graze, to time instantaneously before $(p+n)T$ for an $n$-periodic orbit.) Under these conditions

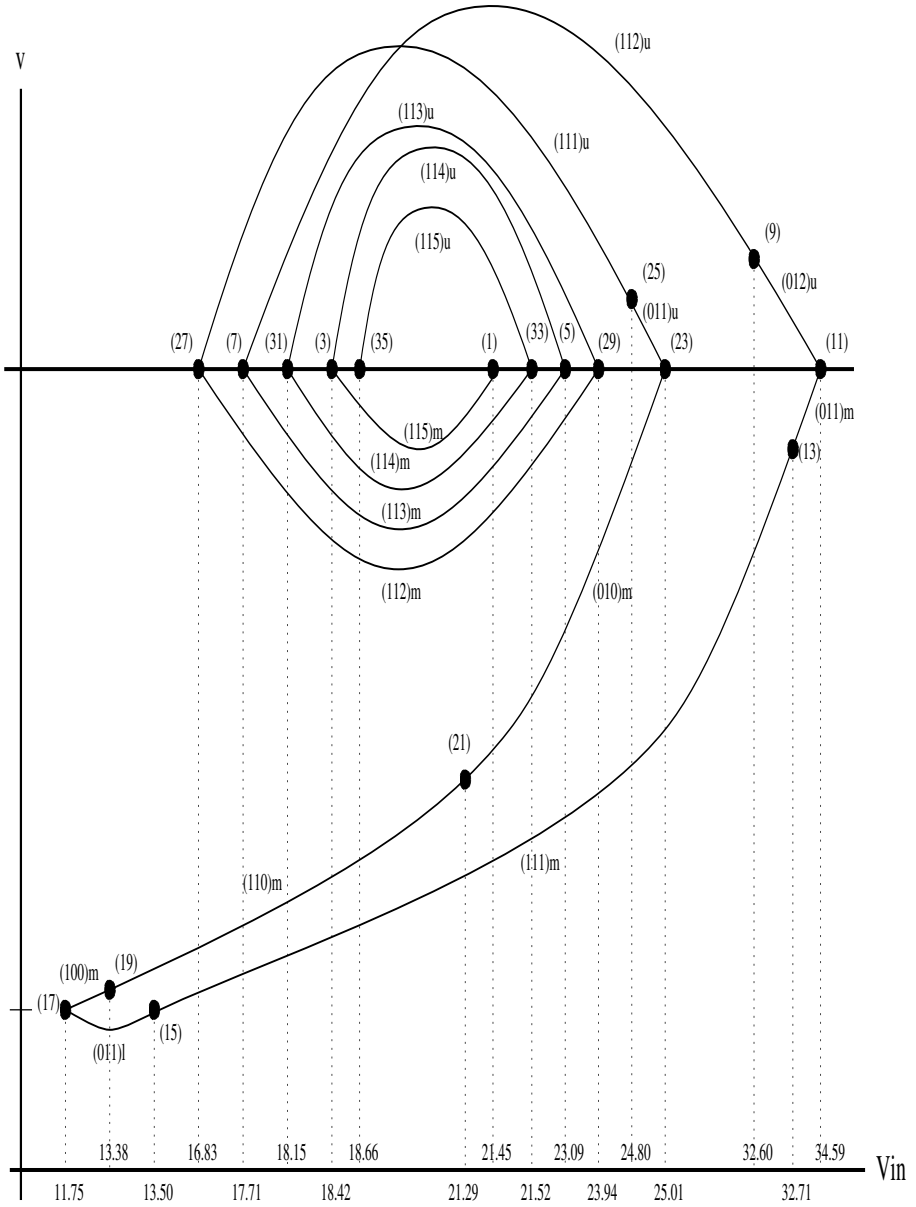


**Figure 10.** (after [6] $O(\cdot, 3)$ Bifurcation diagram. Each grazing bifurcation is represented by a black spot

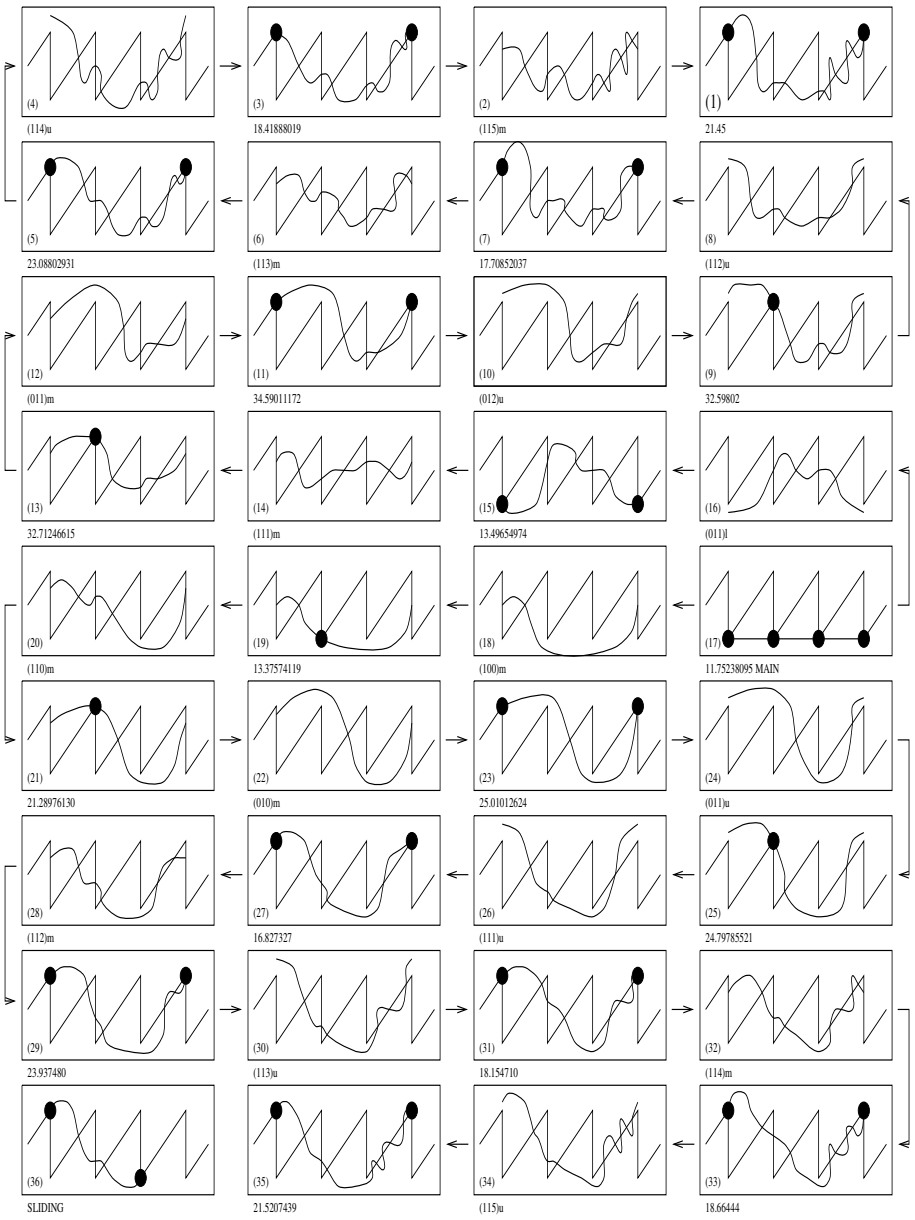


**Figure 11.** (after [6]) Family of $O(\cdot, 3)$ solutions. Each grazing bifurcation is represented by a black spot

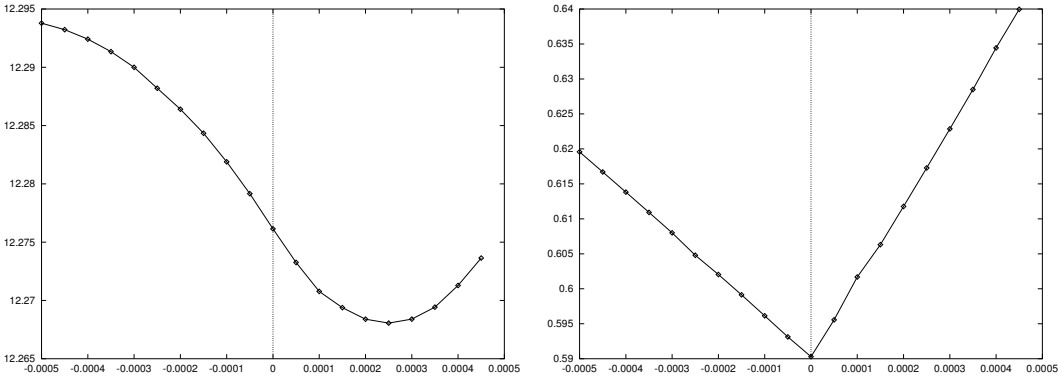


**Figure 12.** Voltage (left) and current (right) local maps, $v(5T)$ and $i(5T)$ vs. $\delta$ as the initial conditions of a five periodic orbit characterised by external grazing are perturbed by an amount $\delta$ $(v_0 \to v_0 + \delta, i_0 \to i_0 + \delta)$.

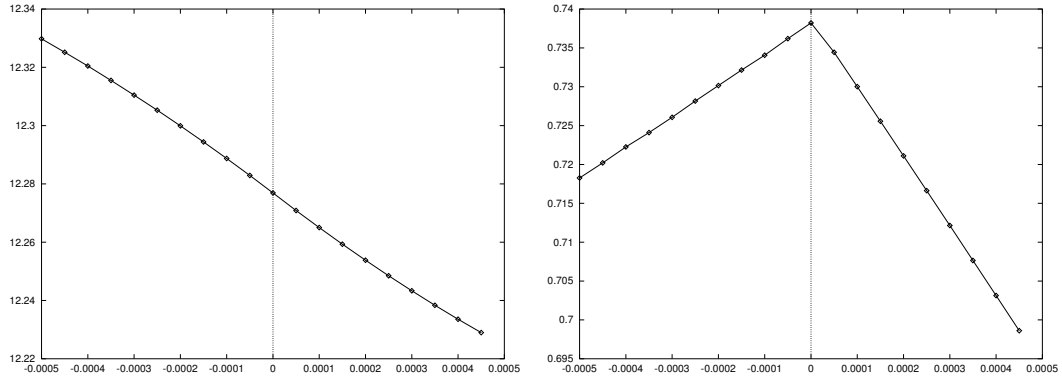


**Figure 13.** Voltage (left) and current (right) local maps, $v(5T)$ and $i(5T)$ vs. $\delta$, as the initial conditions of a five periodic orbit characterized by internal grazing are perturbed by an amount $\delta$ $(v_0 \to v_0 + \delta, i_0 \to i_0 + \delta)$.

we look for fixed points of the map $\Pi_1$ alone, which we assume to take the form

$$x_2 = ax_1 + by_1 + c\mu, \tag{5}$$

$$y_2 = \begin{cases} dx_1 + ey_1, & \text{if } x_2 < 0, \\ gx_1 + hy_1, & \text{if } x_2 > 0 \end{cases} \tag{6}$$

with $a, b, c, d, e, g, h, \mu \in \mathcal{R}$, plus higher order terms, which we ignore in what follows.

For periodic orbits, we seek fixed points of $\Sigma_1 \circ \Sigma_2$. Therefore:

$$y_2 = y_1 = \bar{y}, \quad x_2 = x_1 = \bar{x} \tag{7}$$

and we get:

$$\bar{x} = \frac{b}{1-a}\bar{y} + \frac{c}{1-a}\mu, \tag{8}$$

and

$$\bar{y} = \begin{cases} \hat{a}\bar{y}, & \text{if } \hat{b}\bar{y} + \hat{c}\mu < 0, \\ \hat{d}\bar{y}, & \text{if } \hat{b}\bar{y} + \hat{c}\mu > 0, \end{cases} \tag{9}$$

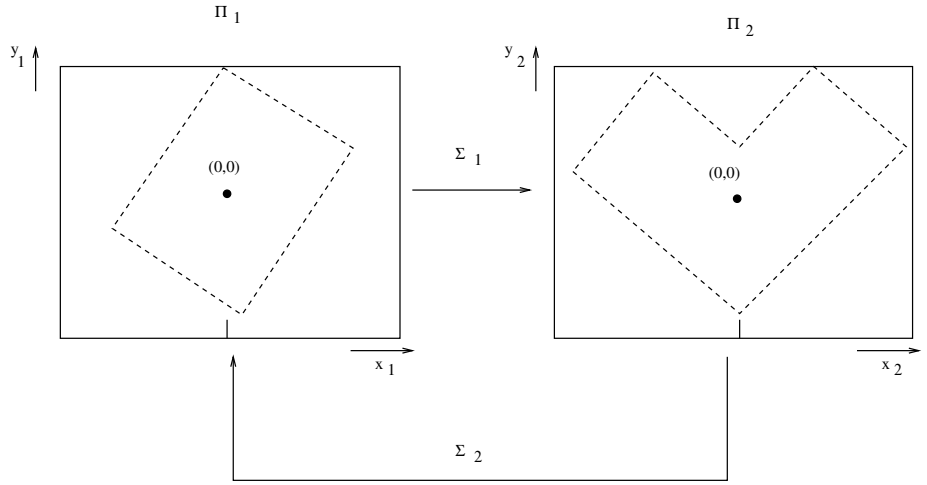


**Figure 14.** Schematic diagram showing the construction of a Poincaré map for external grazing. $\Pi_2$ is taken immediately after the grazing time instant $i(nT+\epsilon), v(nT+\epsilon)$, and $\Pi_1$ is some other Poincaré section local to the periodic orbit away from the grazing instant

where $\hat{a}, \hat{b}, \hat{c}, \hat{d}$ can be obtained from the constants in eq. (6).

Notice that the solutions of equation (9) are strongly dependent on the value of the scaling constants $\hat{a}, \hat{b}, \hat{c}, \hat{d}$ and the map parameter $\mu$. In particular, if $|\hat{a}|, |\hat{d}| > 1$, Eq. 9 will have two solution for $\mu < 0$ and no solution for $\mu > 0$ (see fig. 15).

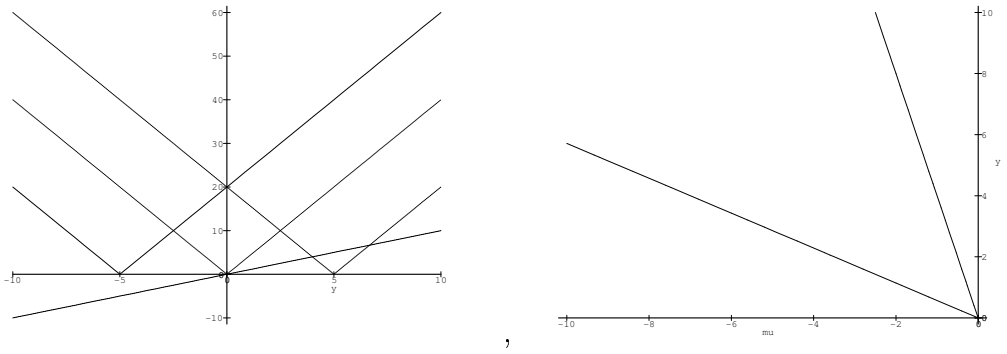


,

**Figure 15.** Local Maps as $\mu$ varies

It is relevant to point out that, as it is clearly outlined in fig. 15, the local bifurcation diagram of the map proposed presents a corner similar to the ones presented in fig. 10. Hence the presence of several sharp turning point in the bifurcation diagram of periodic solutions can be explained as a consequence of several grazing phenomena. In the case of the 3-periodic orbit which grazes at $E = 32.78995$, direct numerical investigation shows that, $|\hat{a}| = 7.8306 > 1, |\hat{d}| = 1.1458 > 1$ hence the existence of corners in the bifurcation diagram as predicted by the analysis.

## 5. Local analysis of sliding and associated dynamics

Following our numerical calculations, it would appear that for certain values of $E$ there are solutions which repeatedly cross over the ramp with small excursions on either side and as $E$ approaches a critical value these excursions tend to zero magnitude and to a solution which switches on and off infinitely often. (A role very similar to homoclinic orbits in the dynamics.) We now seek to obtain such a solution and to consider solutions which lie close to it. This immediately leads us to the derivation of a map relating the voltage and current at the bottom of the ramp to that at the top ($\Sigma_{loc}$), which takes the form of a double spiral (see fig. 16.

We will then derive, in §6, a map from the top of the ramp back to the bottom ($\Sigma_{glob}$) and study its composition with the map described above in order to explain the spiral bifurcation structure outlined in the previous sections.

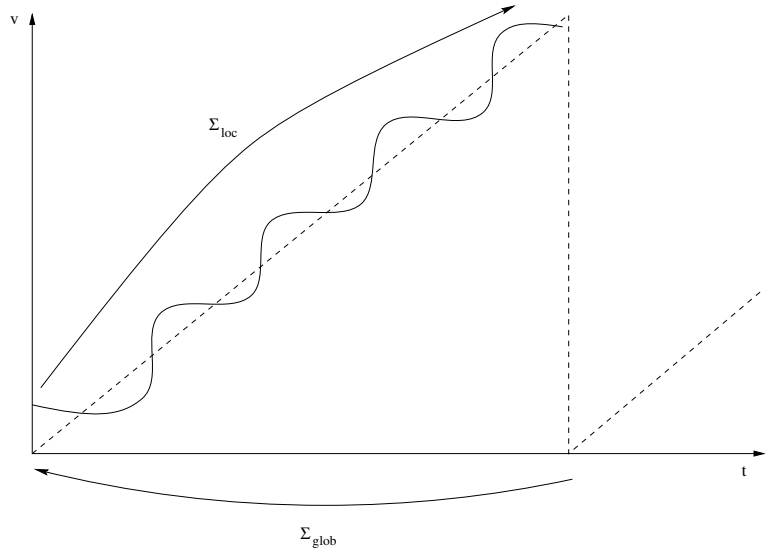


**Figure 16.** Sketch of the two maps from the bottom of the ramp to the top and vice versa

### *5.1. Sliding periodic solutions*

A sliding $n$-periodic orbit is one for which $v(0) = v(nT)$, $i(0) = i(nT)$ and the trajectory coincides for $0 < t < T$ with the part of the switching cycle comprising a ramp

$$v(t) = v_r(t), \qquad 0 \leq t \leq T, \tag{10}$$

where

$$v_r(t) = \gamma + \eta t. \tag{11}$$

Now, it is not difficult to see, in the absence of any additional structure or invariants of systems of the form (2) that such a trajectory should be of co-dimension 2. For example, thinking of the initial condition of a sliding solution at the top of the ramp,

two parameters are required in order for the solution after $(n-1)T$ to satisfy the correct $v$ *and* $i$ to lie tangent to the bottom of the ramp.

By varying two parameters, namely the input voltage $E$ and the load resistance $R$ in (2), we were indeed able to detect several periodic sliding trajectories. In particular, we located a three-periodic sliding solution at $E = 20.328345V, R = 40.178182\Omega$. A five periodic sliding orbit was also found for $E = 34.236729V, R = 21.696801\Omega$.

We therefore conclude that the system (1) with the original parameter values (3) is close, for $E \approx 34.3V$ to a co-dimension-two system containing a 5-periodic sliding trajectory, in the sense that a small perturbation of $(E, R)$ results in a system possessing such a co-dimension-two trajectory. Similarly the 3-periodic region, depicted in fig. 5, for $E \approx 21.0V$ appears to feel the "ghost" of the other sliding solution for $R = 40.178182\Omega$. Numerically we have found evidence that the 3-periodic spiral is much less complete that the 5-periodic one which in the light of the analysis in §5.4 below is consistent with it being further away from the co-dimension-two point.

For the remainder of this section we shall assume that a two-dimensional vector of parameters $(E, R)$ is allowed to vary and that at $(E^s, R^s)$ the system exhibits an $n$-periodic sliding trajectory.

Note that, along a sliding portion of a solution, the differential equation is not properly defined. Presently we will construct a sliding solution as a limit of more classical solutions, but for the moment we presume that such a solution exists and we now look at some of its properties. From the system (1), we have

$$\frac{dv}{dt}(t) = -\frac{v(t)}{RC} + \frac{i(t)}{C} \tag{12}$$

and we immediately have that if $0 \le t \le T$ then for sliding

$$i(t) = i_r(t) = \frac{\gamma}{R} + \frac{\eta t}{R} + \eta C, \tag{13}$$

observing that

$$i(0) = \frac{\gamma}{R} + \eta C, \qquad i(T) = i(0) + \frac{\eta T}{R}. \tag{14}$$

Now from the system equations (2), we have

$$\frac{di}{dt}(t) = -\frac{v(t)}{L} + \frac{E}{L}\xi(t), \tag{15}$$

where $\xi(t) = 1$ if $v(t) < v_r(t)$ and $\xi(t) = 0$ if $v(t) > v_r(t)$.

Eq. (13) does not satisfy (15) as the small excursions of current, which are perturbations of the sliding solution have derivatives which do not tend to zero as $(i(0), v(0)) \to (i_r(0), v_r(0))$. Furthermore it is unclear for a solution satisfying (10) precisely when it is on or off. To resolve this we shall aim to solve eq. (15) in an *averaged* sense by integrating (15) over the period $T$ of the ramp. To do this calculation we assume that during this time the converter is ON for a time interval $\lambda T$ and OFF for the interval $(1-\lambda)T$. Now integrating (15) over the period $T$ and using (10)-(11) and (14) we have

$$\frac{\eta T}{R} = -\frac{\gamma T}{L} - \frac{\eta T^2}{2L} + \frac{E}{L}\lambda T \tag{16}$$

thus

$$\lambda = \frac{1}{E}\left(\frac{\eta L}{R} + \gamma + \frac{\eta T}{2}\right) \tag{17}$$

The predicted $\lambda$ for different values of the input voltage $E$ agrees perfectly with numerical observations, see Table 1.

**Table 1.** Predicted and observed values of $\lambda$ computed along (near) sliding portions of trajectories, for different values of the input voltage $E$.

| Input voltage $E$ | Predicted $\lambda$ | Observed $\lambda$ | No. $A$-switchings detected |
|---|---|---|---|
| 30.00 | 0.4401 | 0.4402 | 899 |
| 32.00 | 0.4126 | 0.4126 | 852 |
| 34.33 | 0.3845 | 0.3842 | 843 |
| 35.00 | 0.3773 | 0.3773 | 861 |
| 40.00 | 0.3300 | 0.3299 | 821 |

To complete our calculation we must determine $(E^s, R^s)$. This we find by looking at the solution after it has left the top of the ramp and solving (1) with the initial conditions

$$i(T) = \frac{\gamma}{R} + \frac{\eta T}{R} + \eta C, \quad v(T) = \gamma + \eta T.$$

The value of $(E^s, R^s)$ is then given by finding values of $(E, R)$ such that for some integer $n$ we have

$$i(nT) = \frac{\gamma}{R} + \eta C, \quad v(nT) = \gamma \tag{18}$$

### *5.2. Solutions close to sliding*

Now we consider the form of those solutions which lie close to a sliding solution. To do this we consider small continuous functions $\alpha(t)$ and $\beta(t)$ so that

$$v(t) = \gamma + \eta t + \alpha(t), \tag{19}$$

$$i(t) = \frac{\gamma}{R} + \frac{\eta t}{R} + \eta C + \beta(t), \tag{20}$$

with $\alpha(t)$ and $\beta(t)$ small. The functions $\alpha(t)$ and $\beta(t)$ have different smoothness properties, in particular as $v(t)$ crosses the ramp $v_r(t)$ the function $\alpha(t)$ has a discontinuous second derivative, and $\beta(t)$ a discontinuous first derivative.

Substituting into Eq. (2) gives

$$\dot{\alpha}(t) = -\frac{\alpha}{RC} + \frac{\beta}{C}, \tag{21}$$

$$\dot{\beta}(t) = -\frac{\alpha}{L} + \frac{E}{L}\xi(t) - \frac{\gamma}{L} - \frac{\eta}{R} - \frac{\eta t}{L}, \tag{22}$$

where now $\xi(t) = 1$ if $\alpha(t) < 0$ and $\xi(t) = 0$ if $\alpha(t) > 0$. Although we can solve (21) and (22) exactly between switchings, the resulting expressions are complex and do not afford much insight. Rather more information is given by an *asymptotic approach.*

To do this presume that at some time $t_0 \in (0, T)$ we have $\alpha(t_0) = 0$ and $\beta(t_0) = \delta > 0$, where $\delta$ is small. From (21) and (22) we have that $\dot{\alpha} > 0$ and the system is thus initially OFF. Whilst $\alpha > 0$ and small, then to the leading order we have from (21) and (22) that

$$\dot{\beta}(t) = -\frac{\gamma}{L} - \frac{\eta}{R} - \frac{\eta t}{L} \equiv -\theta_-(t)$$

where $\theta_-(t) > 0$ is the absolute value of the gradient. Observe that for the parameter values (3) $\eta T/L = 26.190476 \ll \gamma/L + \eta/R = 647.509948$ so that $\dot{\beta}$ is very nearly constant, whilst $\alpha > 0$ . Hence to a very good approximation, we have that, if $\alpha > 0$:

$$\beta(t) = \delta\theta_-(t_0)(t - t_0).$$

If we initially assume that $\alpha \ll \beta$, then integrating (21) and (22) gives

$$\alpha(t) = \frac{1}{C}(t - t_0)\left(\delta - \theta_-(t_0)\frac{(t - t_0)}{2}\right).$$

Observe then that $\alpha(t_1) = 0$ when

$$t = t_1 = t_0 + \frac{2\delta}{\theta_-(t_0)}$$

and during the interval $t_0 \leq t \leq t_1$, $\alpha(t)$ takes the maximum value

$$\alpha_{\max} = \frac{\delta^2}{2C\theta_-}.$$

For $\delta \ll 1$ this is consistent with the original assumptions made on $\alpha(t)$. Moreover at $t = t_1$ we have simply that $\beta(t) = -\delta$. Over this "half cycle" we thus have figures of $\alpha(t)$ and $\beta(t)$ as depicted in Fig. 17.

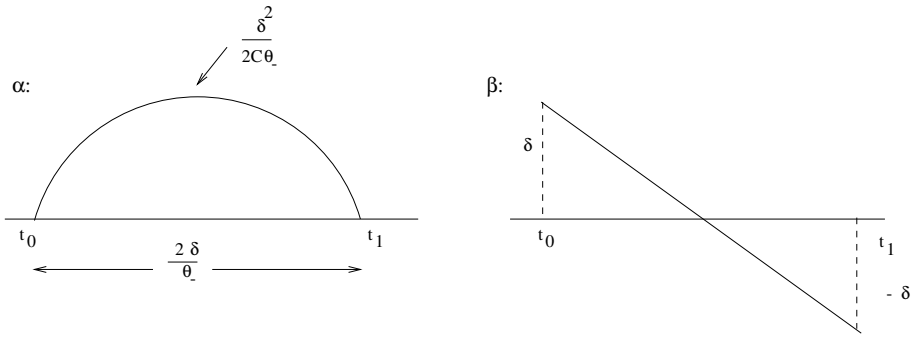


**Figure 17.** Evolution of $\alpha(t)$ and $\beta(t)$ over the *half cycle* $(t_0, t_1)$

For $t > t_1$ the value of $\alpha(t)$ becomes negative and the system switches ON. In this case the gradient of $\beta$ changes from negative to positive.

Repeating the previous arguments gives

$$\alpha(t) = \frac{1}{C}(t - t_1)(\theta_+(t_1)\frac{(t - t_1)}{2} - \delta)$$

and

$$\beta(t) = -\delta + \theta_+(t_1)(t - t_1),$$

with

$$\theta_+(t) = \frac{E}{L} - \frac{\gamma}{L} - \frac{\eta}{R} - \frac{\eta t}{L},$$

where we note (significantly) that $\theta_+(t) > 0$ for the parameter values (3).

In this case we have $\alpha(t_2) = 0$ where

$$t_2 = t_1 + \frac{2\delta}{\theta_+(t_1)}$$

and $\|\alpha\|$ takes its maximum value of

$$\|\alpha\|_{\max} = \frac{\delta^2}{2C\theta_+}.$$

The complete picture of functions $\alpha$ and $\beta$ in the interval $t \in (t_0, t_2)$ is then as reported in Fig. 18.

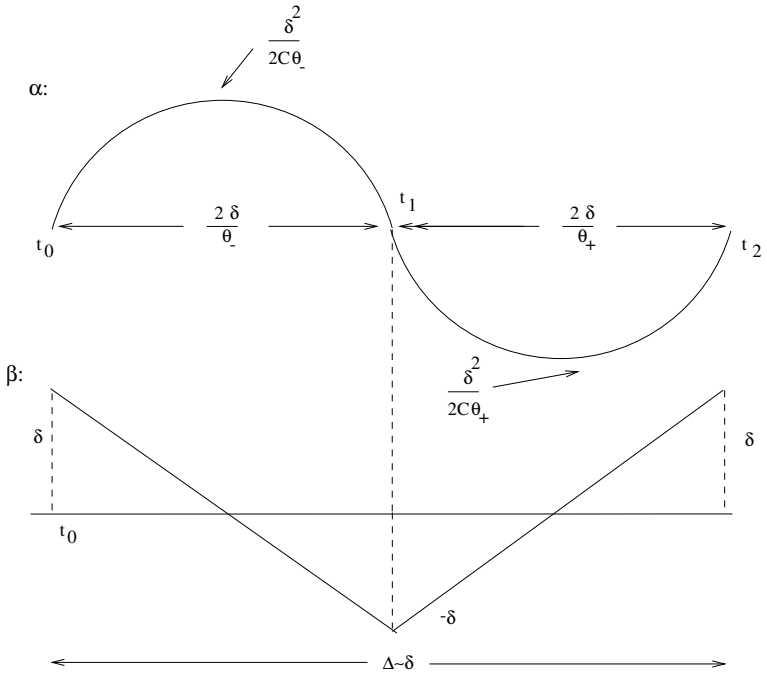


**Figure 18.** Evolution of $\alpha(t)$ and $\beta(t)$ over $(t_0, t_2)$, showing their scalings as functions of $\delta$.

The oscillations then repeat from $t = t_2$ with a slightly larger value of $\theta_-$ and a slightly smaller value of $\theta_+$. Observe that during the ramp cycle $\theta_-$ and $\theta_+$ only vary slightly from the mean values of

$$\theta_- = \frac{\gamma}{L} + \frac{\eta}{R} + \frac{\eta T}{2L} \tag{23}$$

and

$$\theta_+ = \frac{E}{L} - \frac{\gamma}{L} - \frac{\eta}{R} - \frac{\eta T}{2L} \tag{24}$$

Thus we see that the nature of a solution close to sliding is one which oscillates either side of the sliding solution and which has a small amplitude $\delta$ in $\beta$ and an asymptotically much smaller amplitude of $\delta^2/(2C\theta_-)$ or $\delta^2/(2C\theta_+)$ in $\alpha$. The

"wavelength" of the oscillation decreases with amplitude and has the mean value of $\Delta$, where

$$\Delta = \frac{2\delta}{\theta_+} + \frac{2\delta}{\theta_-} = \frac{2\delta(\theta_+ + \theta_-)}{\theta_+\theta_-},$$

which using (23)-(24) gives

$$\Delta = \frac{2\delta E}{L} \frac{1}{(\frac{\gamma}{L} + \frac{\eta}{R} + \frac{\eta T}{2L})(\frac{E}{L} - \frac{\gamma}{L} - \frac{\eta}{R} - \frac{\eta T}{2L})}. \tag{25}$$

Note that $\Delta$ is proportional to $\delta$ and hence the number of switchings during the period $0 \leq t \leq T$ is proportional to $1/\delta$.

The mean time spent ON is then

$$\frac{1}{\Delta}\frac{2\delta}{\theta_+} = \frac{\theta_-}{\theta_+ + \theta_-} = \frac{1}{E}\left(\gamma + \frac{\eta L}{R} + \frac{\eta T}{2}\right),$$

which is precisely the value of $\lambda T$ calculated via (17).

### *5.3. Derivation of the local map*

By using the results of the previous section we can now derive a map from $v(0)$ and $i(0)$ to $v(T)$ and $i(T)$, by looking in a neighbourhood of the sliding solution.

If

$$v(0) = \gamma, \quad i(0) = \frac{\gamma}{R} + \eta C,$$

then we are on the sliding solution and consequently

$$v(T) = \gamma + \eta T, \quad i(T) = \frac{\gamma}{R} + \eta C + \frac{\eta T}{R}.$$

We now consider the effect of making small perturbations to the above initial conditions. To do this set

$$v(0) = \gamma + v_i, \quad i(0) = \frac{\gamma}{R} + \eta C + i_i$$

and

$$v(T) = \gamma + \eta T + v_f, \quad i(T) = \frac{\gamma}{R} + \eta C + \frac{\eta T}{R} + i_f,$$

where $v_f$ and $i_f$ are presumed small.

Let $\Pi_1$ be the local Poincaré section $t = 0^+ (\text{mod } T)$ with co-ordinates $(i_i, v_i)$, and $\Pi_2$ be the local Poincaré section $t = 0^- \ (\text{mod } T)$ with co-ordinates $(i_f, v_f)$. Then suppose that the map from the bottom of the ramp to the top in a neighbourhood of sliding takes the form

$$\Sigma_{loc} : \Pi_1 \to \Pi_2, \quad (i_i, v_i) \mapsto (i_f, v_f) = (I(i_i, v_i), V(i_i, v_i)) \,. \tag{26}$$

In what follows we determine the zeros and asymptotic scaling of $I$ and $V$ in the three separate cases when $i_i$, $v_i$, or both are varied by an amount $\delta > 0$.

*5.3.1. Case I; $i_i$ varying* Suppose now that we set $v_i = 0$ and vary $i_i$ through an interval which includes 0. This is of course equivalent to setting $t_0 = 0$ in the previous calculations and $i_i = \delta$.

Initially take $\delta > 0$. As $\delta$ is reduced there will be a first value $\delta_N$ such that for a given integer $N$

$$T = N\Delta.$$

From Eq. (25) we see that there is a constant $\mu$ such that

$$T = 2N\delta(\theta_+ + \theta_-)\frac{1}{\theta_+\theta_-} \equiv \mu\delta_N N,$$

so that

$$\delta_N = \frac{T}{\mu N}.$$

For this value of $\delta_N$ we have simply that

$$v_f(T) = 0, \quad i_f(T) = \delta_N,$$

as the system has an integer number of excursions either side of the sliding solution.

Now if $\delta$ is reduced there is a first value $\delta_{N+\frac{1}{2}}$ such that

$$T = N\Delta + \frac{2\delta_{N+\frac{1}{2}}}{\theta_+},$$

so that

$$\delta_{N+\frac{1}{2}} = \frac{T}{\mu N + \frac{2}{\theta_+}}.$$

In the interval $\delta_{N+\frac{1}{2}} < \delta < \delta_N$ the deviation of $\alpha$ from zero goes through a half cycle with $\alpha < 0$. At the end of this half cycle $\alpha(T) = 0$, thus at $\delta_{N+\frac{1}{2}}$

$$v_f(T) = 0, \quad i_f(T) = -\delta_{N+\frac{1}{2}}.$$

At an approximate mid-point $\delta_{N+\frac{1}{4}}$ satisfying

$$\delta_{N+\frac{1}{4}} = \frac{T}{\mu N + \frac{1}{\theta_+}},$$

the value of $\|\alpha\|$ takes its maximum value, so that at this value of $\delta$

$$v_f(T) = -\frac{1}{2C\theta_+}\delta^2_{N+\frac{1}{4}}, \quad i_f(T) = 0.$$

If $\delta$ is now reduced to $\delta_{N+1}$ similar behaviour occurs except that $\alpha > 0$. Combining these results gives an element of a spiralling structure on the $(v_f, i_f)$ plane if $\delta_{N+1} < \delta < \delta_N$, as detailed in Fig. 19 and 20.

If we let $\delta \mapsto 0$ then this sequence repeats through all (sufficiently large) integer values of $N$.

Now consider the case of $\delta < 0$. The curves of $\alpha$ and $\beta$ are basically the same though displaced through half a cycle. In this case the values of $\delta_N^-$ play the same role as the earlier values of $\delta_N^+$ with

$$\delta_N^- = -\frac{1}{\mu N} = -\delta_N^+,$$

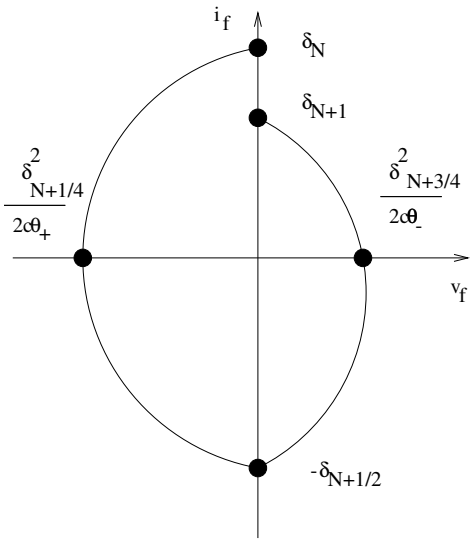


**Figure 19.** Element of the spiralling structure as predicted by the analysis, where $\delta_N = T/(\mu N)$, $\delta_{N+1/4} = T/(\mu N + 1/\theta_+)$, $\delta_{N+1/2} = T/(\mu N + 2/\theta_+)$, $\delta_{N+3/4} = T/(\mu N + 2/\theta_+ + 1/\theta_-)$

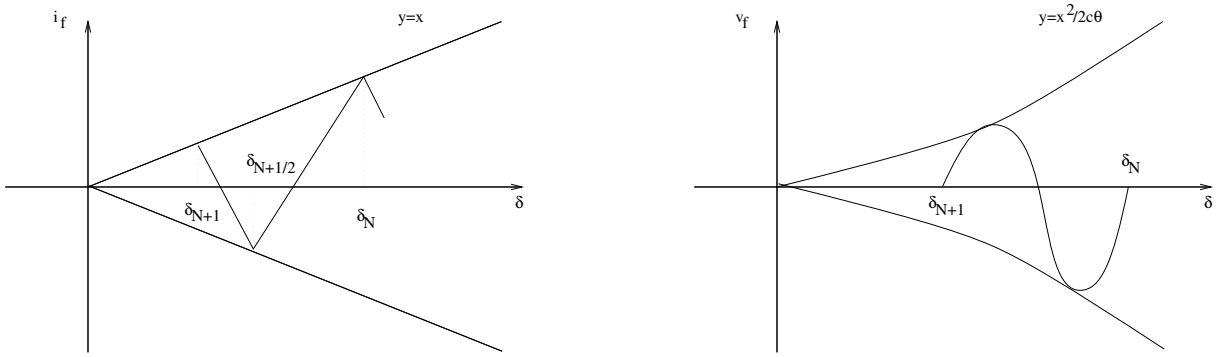


**Figure 20.** $i_f$ and $v_f$ evolution as functions of $\delta$ as predicted by the analysis

in that they are values of $\delta$ for which there is an integer number of oscillations such that if $\delta = \delta_N$ then $v_f(T) = 0$ and $i_f(T) = \delta_N$.

In this case we have

$$\delta^-_{N+\frac{1}{4}} = -\frac{1}{(\mu N + 1/\theta_-)}, \tag{27}$$

$$\delta^-_{N+\frac{1}{2}} = -\frac{1}{(\mu N + 2/\theta_-)}, \tag{28}$$

$$\delta^-_{N+\frac{3}{4}} = -\frac{1}{(\mu N + 2/\theta_- + 1/\theta_+)}, \tag{29}$$

with $v_f(\delta_{N+\frac{1}{2}}) = 0$, $i_f(\delta_{N+\frac{1}{2}}) = -\delta^-_{N+\frac{1}{2}}$, $v_f(\delta_{N+\frac{1}{4}}) = -\delta^2_{N+\frac{1}{4}}/(2C\theta_-)$, $i_f(\delta_{N+\frac{1}{4}}) = 0$, $v_f(\delta_{N+\frac{3}{4}}) = \delta^2_{N+\frac{3}{4}}/(2C\theta_+)$, $i_f(\delta_{N+\frac{3}{4}}) = 0$.

Combining this with the previous results we find that by varying $\delta$ through an

interval which includes zero we trace out an (elegant) double spiral in the $(v_f, i_f)$ plane, as depicted in Figs. 21, 22.

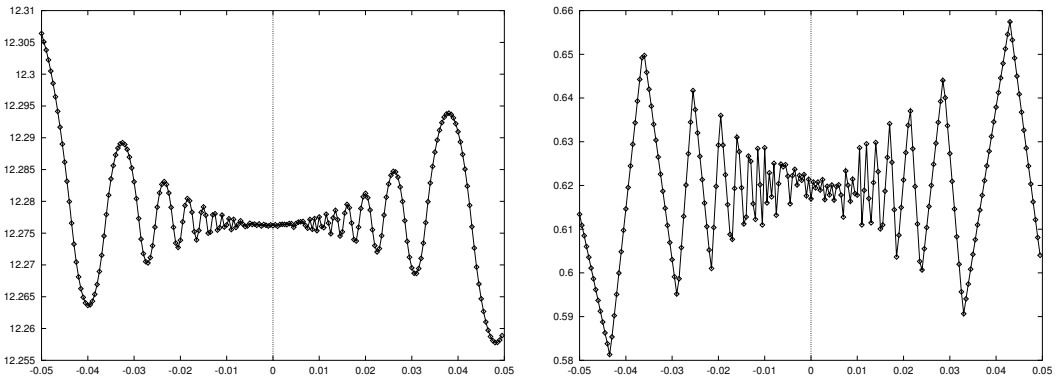


**Figure 21.** Voltage (left) and current (right) evolution at the top of the ramp as $i_i$ is varied while $v_i = 0$ . This figure was calculated using equation (1) at the parameter values near to sliding (3) with $E = 34.339922$.

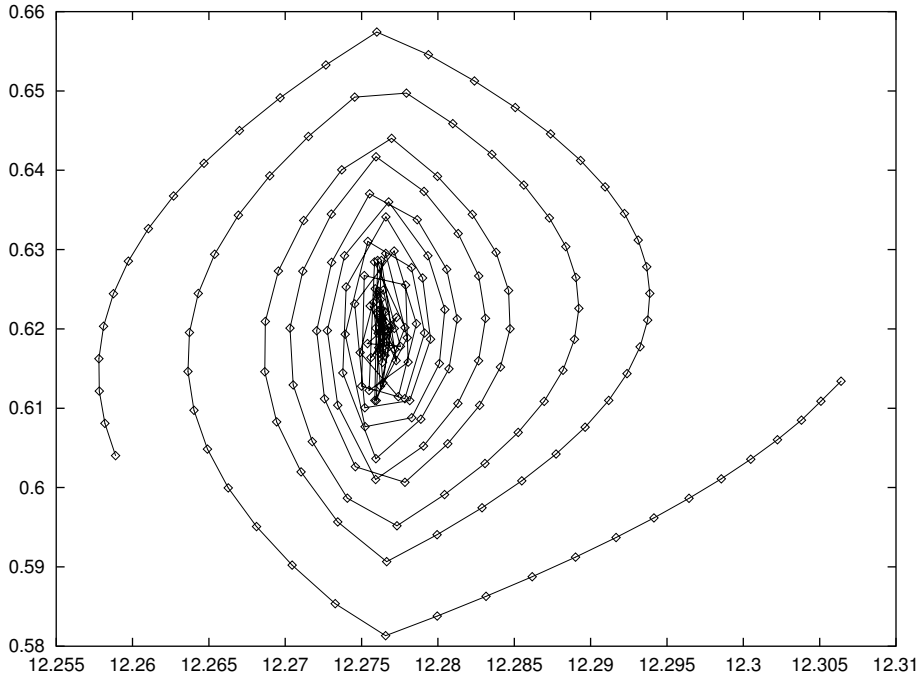


**Figure 22.** Double spiral traced by in the $(v_f, i_f)$ plane when $i_i$ is varied and $v_i = 0$. Computed similarly to figure 21

*5.3.2. Case II; $v_i$ varying* Suppose now that we fix $i_i$ at 0 and vary $v_i$ (see Fig. 23). From our previous analysis it follows that if $v_i > 0$ then $v_i = \delta^2/(2C\theta_-)$. Hence, setting

$$\delta = \sqrt{2C\theta V_i} > 0,$$

we reduce this to previous calculations. Similarly if $v_i < 0$ then set

$$\delta = -\sqrt{-2C\theta V_i} < 0$$

to obtain the other half of the spiral. the double spiral bifurcation diagram is as before and maps from $v_i$ to $v_f$. Fig. 23 shows the voltage and current evolution as $v_i$ is varied.

*5.3.3. Case III; general initial condition* Now suppose that we vary $i_i$ and $v_i$ in a more general way then for some $t_0$ we have (if $v_i > 0$):

$$v - i = \frac{1}{C}(t - t_0)(\delta - \frac{\theta_-}{2}(t - t_0)),$$

$$i_i = \delta - \theta_-(t - t_0),$$

for $\delta$ and $t_0$ to be determined, where $0 < t_0 < 2\delta/\theta_-$ and we can put $t = 0$.

Rearranging we have simply

$$\delta = \sqrt{i_i^2 + 2C\theta_- v_i}, \tag{30}$$

with $t_0$ given by

$$t_0 = \frac{(i_i - \delta)}{\theta_-}.$$

If $v_i < 0$ then similarly

$$\delta = \sqrt{i_i^2 - 2C\theta_+ v_i}. \tag{31}$$

In what follows we will refer to

$$\delta = \sqrt{i_i^2 + \Theta(v_i)},$$

where

$$0 < \Theta(v_i) = \begin{cases} 2C\theta_- v_i, & \text{if } v_i > 0 \\ -2C\theta_+ v_i, & \text{if } v_i < 0 \end{cases}. \tag{32}$$

We can now use the results of the previous calculation to compute the desired map. Here $\delta$ is proportional to the magnitude of $i_f$ and $\delta^2$ to that of $v_f$. The value of $t_0$ gives the phase of a point on the double spiral (which is less significant than the value of $\delta$). Note from (30) that if $i_i$ and $v_i$ are of comparable small magnitude then $\delta$ is asymptotically dependent upon $v_i$ alone. This result is important when combining this map from the bottom of the ramp to the top with a subsequent global map from the top of the ramp back to the bottom, as conducted in the next subsection.

### *5.4. The global map and existence of periodic solutions*

We now consider the effect of the global dynamics from $\Pi_2 \to \Pi_1$ over $(n-1)$ periods in a neighbourhood of an $n$-periodic sliding trajectory. It is a numerical observation that we can choose a sufficiently small neighbourhood of such a trajectory in both parameter and phase space such that the dynamics in this neighbourhood do not undergo any grazings except in the period of the ramp cycle which corresponds to

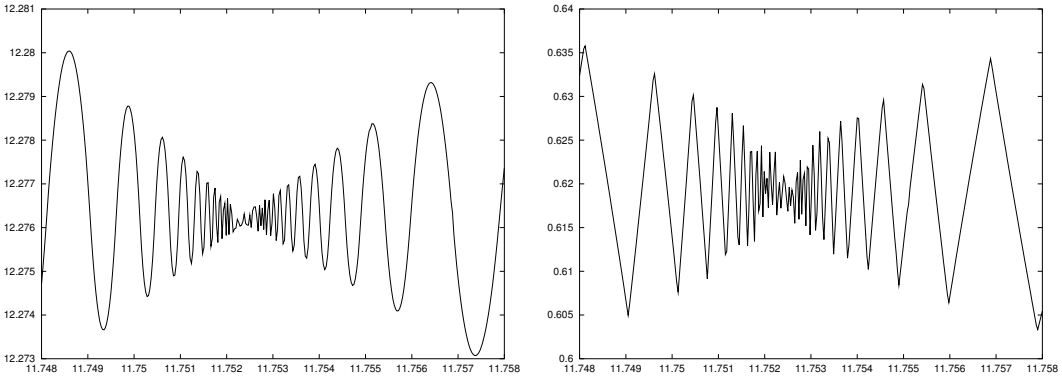


**Figure 23.** Voltage (left) and current (right) evolution at the top of the ramp as $v_i$ is varied. Computed similarly to figure 21

the sliding portion of the orbit. Hence, the number of switchings over the $(n-1)$ remains constant and the global map $\Sigma_{glob} : \Pi_2 \to \Pi_1$ is a diffeomorphism which we can approximate to sufficient accuracy by its linear terms, see fig. 16.

$$\Sigma_{glob} : \Pi_2 \to \Pi_1, \quad \begin{pmatrix} i_i \\ v_i \end{pmatrix} = A \begin{pmatrix} i_f \\ v_f \end{pmatrix} + B \begin{pmatrix} \mu_1 \\ \mu_2 \end{pmatrix}, \tag{33}$$

where $\mu_1 = E - E^s$ and $\mu_2 = R - R^s$.

For the 5-periodic sliding orbit computed earlier at $E = 34.236729, R = 21.696802$ we find that

$$A = \begin{pmatrix} -0.25 & 0.43 \\ -0.49 & 0.0 \end{pmatrix}$$

and

$$B = \begin{pmatrix} 0.025 & -0.018 \\ 0.025 & -0.015 \end{pmatrix}.$$

Note that $A$ and $B$ are non-singular which is all that is required for the linear approximation of $\Sigma_{glob}$ to be valid.

In order to seek periodic solutions in a neighbourhood of sliding we consider fixed points of $\Sigma_{glob} \circ \Sigma_{loc}$. Since $\theta^{\pm}$ are approximately constant, it is reasonable to assume that the functions $I$ and $V$ in (26) are parameter independent, and that all parameter dependence appears via the matrix $B$ in (33). Hence, we get

$$\Sigma_{glob} \circ \Sigma_{loc} : \begin{pmatrix} i_i^{(2)} \\ v_i^{(2)} \end{pmatrix} \mapsto A \begin{pmatrix} I(i_i^{(1)}, v_i^{(1)}) \\ V(i_i^{(1)}, v_i^{(1)}) \end{pmatrix} + B \begin{pmatrix} \mu_1 \\ \mu_2 \end{pmatrix}, \tag{34}$$

Notice that when we perturb a sliding solution ($v_i = 0, i_i = 0$) by an amount $\delta$ given by (31) we can write that

$$I(i_i, v_i) \approx \mathcal{I}(\delta), \quad V(i_i, v_i) \approx \mathcal{V}(\delta) \tag{35}$$

where with $\mathcal{I}$ and $\mathcal{V}$ we indicate the functions $I$ and $V$ as functions of $\delta$. Now, recall from the scalings (30), (31) and the form of $I$ and $V$ that for $\mu_1 = \mu_2 = 0$,

$$\limsup \mathcal{I} = \mathcal{O}(\delta), \quad \limsup \mathcal{V} = \mathcal{O}(\delta^2), \quad \text{as } \delta \to 0,$$

where

$$\delta = \sqrt{i_i^2 + \Theta(v_i)}.$$

Looking for periodic orbits in a neighbourhood of the sliding solution, we set

$$i_i^{(1)} = i_i^{(2)} = \bar{i}, \quad v_i^{(2)} = v_i^{(2)} = \bar{v}.$$

Substituted into (34), this yields, to lowest order in $\delta$,

$$\begin{aligned} \bar{i} &= a_{11}\mathcal{I}(\bar{\delta}) + b_{11}\mu_1 + b_{12}\mu_2 + O(\delta^2), \\ \bar{v} &= a_{21}\mathcal{I}(\bar{\delta}) + b_{21}\mu_1 + b_{22}\mu_2 + O(\delta^2), \end{aligned}$$

where $\bar{\delta} = \sqrt{\bar{i}^2 + \Theta(\bar{v})}$. Thus, we obtain

$$\bar{v}) - b_{21}\mu_1 - b_{22}\mu_2 = a_{21}\mathcal{I}\left(\sqrt{(b_{11}\mu_1 + b_{12}\mu_2)^2 + \Theta\bar{v} + O(\delta)}\right) + O(\delta^2). \qquad (36)$$

Note that the right hand side for $\mu_1 = \mu_2 = 0$ is proportional to $I(\bar{v})$ plotted in Figure 23 and scales as $\sqrt{\bar{v}}$ as $\bar{v} \to 0$.

To explain the observed dynamics of either the 3-periodic or 5-periodic spiral bifurcation diagram observed in §3, we consider solutions of (36) for $\mu_2 = R - R^s \neq 0$ as fixed and consider the effect of varying $\mu_1 = E - E^*$ through zero. Fig. 24 shows sketches of the left-hand side versus the right-hand side for three different values of $E$. The analysis of fixed points then follows a similar argument to that of the 1-D map arising in Shil'nikov homoclinic bifurcations [14]. Each time the straight line representing the left-hand side passes through a corner in the graph of the right-hand side we must have a grazing bifurcation. Also, intersections towards $v_i = 0$ naturally imply a greater number of intersections with the ramp. Therefore we conclude that the bifurcation diagram looks like Fig. 25. Note that the double spiral is incomplete. If instead we had considered a ray in parameter space that passed precisely through $E^s, R^s$ then we would find a perfect, complete double spiral.

We will now derive the scalings of the intersections between the spiral and the $E$-axis in fig. 25. These intersections are given by the points in fig. 24 at which the left-hand side and the right-hand side of eq. (36) become tangent, which from the geometry of the right-hand side occurs at the corner of the piecewise linear function $\mathcal{I}$. We will refer to the values related to these points by using the subscript $i$.

From the analysis presented in the previous section we know that $\mathcal{I} \sim \delta$, hence from eq. (36) we obtain, to lowest order:

$$\bar{v}_i - b_{21}\mu_1 - b_{22}\mu_2 \simeq k\delta_i \qquad (37)$$

where

$$\delta_i^2 = (b_{11}\mu_1 + b_{12}\mu_2)^2 + \Theta(\bar{v}_i) \qquad (38)$$

as given by eq. (31). From eq. (37) and eq. (32) we then obtain:

$$\frac{\delta_i^2 - (b_{11}\mu_1 + b_{12}\mu_2)^2}{\pm 2C\theta_{\mp}} = k\delta_i + b_{21}\mu_1 + b_{22}\mu_2 \qquad (39)$$

Hence, if we vary only $\mu_1$ while keeping $\mu_2$ fixed, as in the case of the spiral diagram actually observed in the experimental circuit, we can conclude that the value $\mu_1^i$ at which an intersection occur is given by:

$$\mu_1^i \simeq K\delta_i + C\mu_2 + \mathcal{O}(\mu_2\delta_i, \delta_i^2, \mu_2^2)$$

where $K$ and $C$ are constants easily obtained as combination of the constants in (39).

So until $\delta \gg \mu_2$ (i.e. far enough from the sliding point) we get that two successive intersections on one side of the spiral scale as:

$$\frac{\mu_1^{i+1}}{\mu_1^i} = \frac{\delta_{i+1} + C\mu_2}{\delta_i + C\mu_2} \approx \frac{\delta_{i+1}}{\delta_i} \tag{40}$$

Finally from the analysis reported in the previous section we know that $\delta \sim 1/N$ therefore we get:

$$\frac{\mu_1^{i+1}}{\mu_1^i} \sim \frac{N_i}{N_{i+1}} = 1 - \frac{2}{N_i + 2} \tag{41}$$

where $N_i$ is the number of switching characterising the last period of the periodic solution undergoing a grazing (corner) as we unfold the sliding orbit. Notice that $N_{i+1} = N_i + 2$ in the double spiral considered (see fig. 10). Also, we get

$$\frac{\mu_{i+1} - \mu_i}{\mu_i - \mu_{i-1}} \approx \frac{\delta_{i+1} - \delta_i}{\delta_i - \delta_{i-1}} \approx 1 - \frac{4}{N_i + 2} \tag{42}$$

which characterized how the intersections of the spiral with the $E$-axis scale as we approach the sliding point.

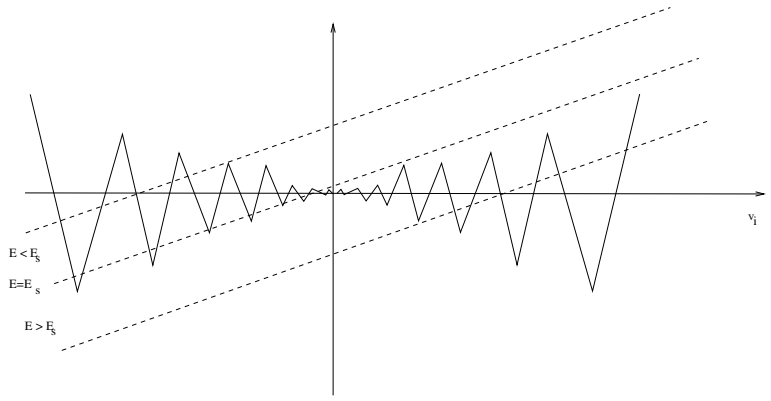


**Figure 24.** Left hand side (dashed line) vs right-hand side (solid line) of eq. (36) as $E$ is varied

Some preliminary numerical results indicate that these scalings are indeed observed in the system (1) with parameter values (3). Consider for instance the grazings occurring at the corners of the 3-periodic spiral, labelled $27, 31$ and $35$ in Fig. 10, which we will name with the subscripts $1, 2$ and $3$ respectively. Since the centre of the double spiral is located at $E_s \simeq 19.975$, we have $\mu_1 = E_1 - E_s = 3.147674$ and similarly $\mu_2 = 1.820289, \mu_3 = 1.3106$. Then,

$$\frac{\mu_2}{\mu_1} = 0.578, \quad \frac{\mu_3}{\mu_2} = 0.72$$

which compare well with the predicted values from eq. (41) of 0.5 and 0.67 respectively $(N_1 = 2, N_2 = 4)$. Also,

$$\frac{\mu_3 - \mu_2}{\mu_2 - \mu_1} = 0.383$$

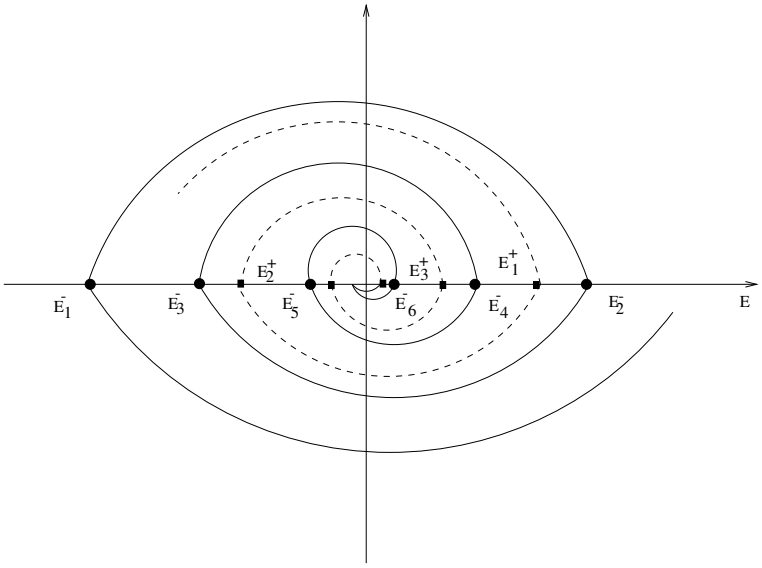


**Figure 25.** Incomplete double spiral bifurcation diagram. The intersections of the spirals, $E_i^+, E_i^-$ obey the scalings (41) and (42).

where the analysis predicts a value of 0.333. These comparisons are good given that the orbits are still far from the sliding solutions. A more careful and extensive computation of these scalings for the 5-periodic spiral is in progress and will be reported elsewhere.

## 6. Strange Attractors

The analysis of the previous subsection can easily be extended to show the existence of Smale horseshoe dynamics on $m$ symbols where $m(E)$ is the maximum number of intersections with the ramp of periodic solutions within the spiral at a particular $E$ value (cf. the corresponding analysis of Shil'nikov homoclinic bifurcations [13]). It would seem that the re-injection mechanism over 5 periods causes this dynamics to be stable. The two questions left to be explained are the sudden jump into this 5-zone attractor at $E \approx 32.342$ and the fingered structure of this chaotic attractor.

### *6.1. The jump to large scale chaos*

From the analysis and the numerical evidence presented in the previous sections we can certainly conclude that a double spiral bifurcation diagram of five periodic orbits is coexisting with the main bifurcation branch when the system evolution jumps onto the 5-zone attractor depicted in fig. 6.

As first conjectured in [5, 6], we note that such jump occurs when the chaotic evolution resulting from the period doubling cascade first grazes the ramp externally. When this occurs, the chaotic evolution starts to feel the influence of the family of five periodic unstable solutions organised around the double spiral bifurcation diagram represented in Fig. 9. These orbits are characterized by multiple $A$-switchings and skippings hence as confirmed by fig. 26, the number of skippings per period suddenly becomes different from zero as we cross the jump bifurcation value.

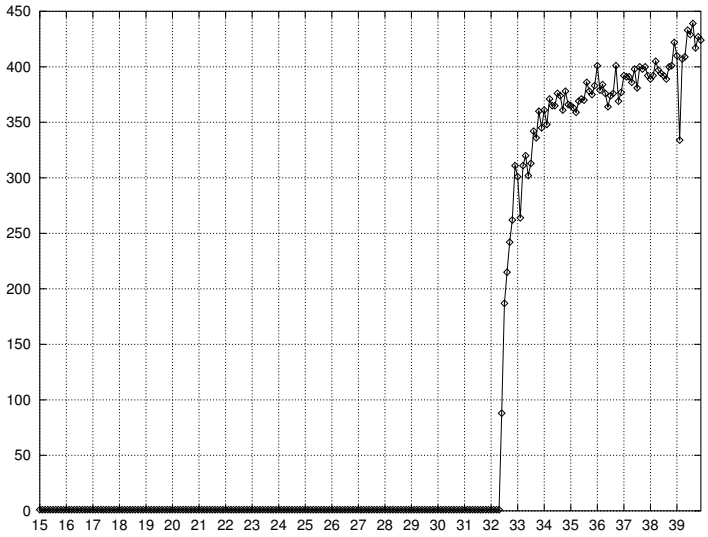


**Figure 26.** Number of skippings over 2000 periods as the input voltage $E$ is varied [6]

Also in Fig. 27, the chaotic attractor before and after the jump is shown for different values of the input voltage $E$. We can see that the attractor before the enlargement takes place, is located in a relatively small scale of the phase plane. As $E$ is increased skippings will become more and more frequent as the fractal edge of the chaotic attractor approaches more and more closely the vertical line corresponding in fig. 27 to skipping. Hence in this system the jump to chaos cannot be characterized by a large-scale bifurcation (e.g. grazing) if a single periodic orbit. Rather, the jump occurs at the parameter value for which the invariant measure of the portion of the chaotic attractor that crosses the skipping line becomes positive. Thus accurately detecting numerically the parameter value of the jump is fraught with difficulty.

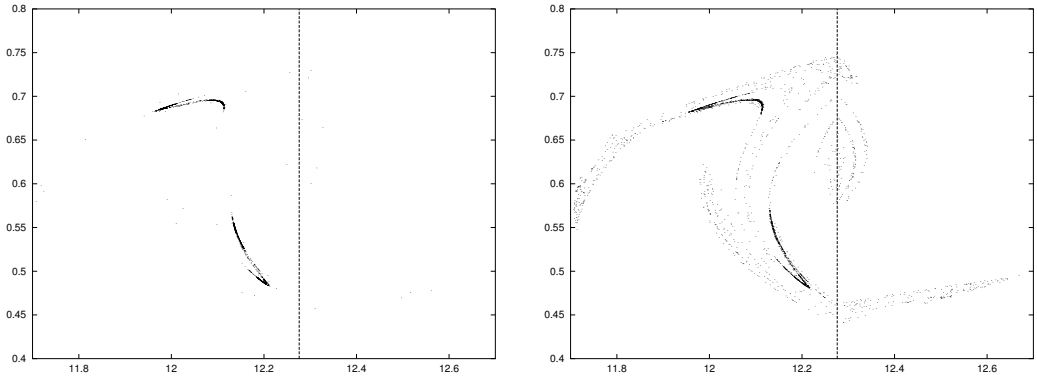


**Figure 27.** Chaotic attractor before ($E = 32.34V$) and after ($E = 32.40V$) the sudden enlargement. The influence of the five-zone large scale attractor is clearly visible

*6.2. The fingered structure*

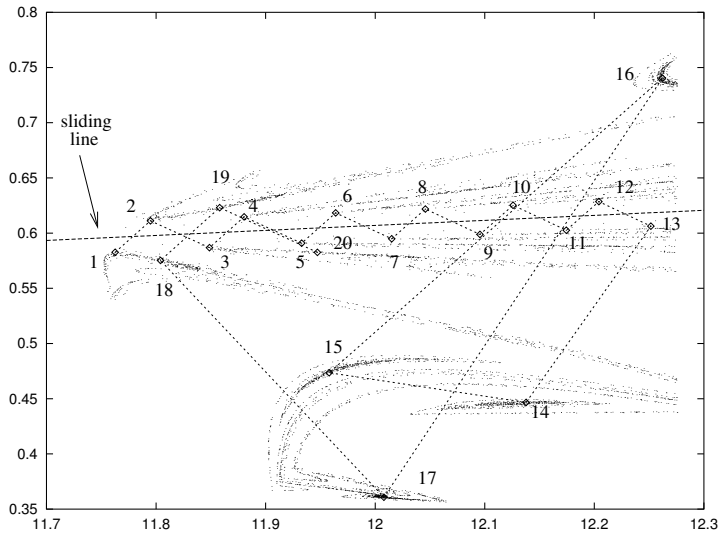


**Figure 28.** Chaotic attractor for $E = 35V$ and $R = 22.0\Omega$ on the $A$-switching map. The fingered structure is visible together with the iterates of a typical trajectory

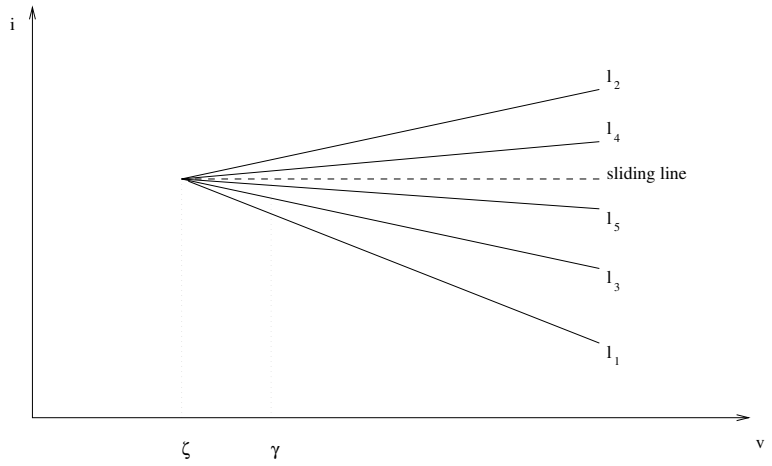


**Figure 29.** Schematic representation of the fingered structure of the attractor when observed on the $A$-switching map

The strange attractor resulting from the mechanism described above has, for values of $E$ close to $E_s$, a very distinctive fingered structure. The attractor is presented in fig. 28 in the case of $E = 35.0V$ and $R = 22.0\Omega$ together with a sequence of iterations of a single point. For this structure the basic features can be described schematically as in fig. 29, where $l_i$, $i = 1..\infty$ represent a sequence of fingers each of which has a fractal form in cross-section. On this schematic an iterate which has a sequence of $A$-switchings on the ramp, has its first switching at a point on $l_1$, its second on $l_2$,

its third on $l_3$ and continues on this sequence until it leaves the ramp and returns through the action of the map $\Sigma_{glob}$.

There are two distinctive features of this schematic

(i) each of the fingers is a straight line of defined gradient;

(ii) the fingers when projected back intersect at a point on the sliding line at a voltage value $\zeta < \gamma$ (even though iterates only lie on the fingers for $v > \gamma$.

Further numerical calculations show that as $E \to E_s$

- the gradients of the fingers stay the same;
- $\zeta$ tends to $\gamma$.

We now make the following assertion that, if $m_i$ is the gradient of the finger $l_i$ then

$$m_1 = \frac{1}{R} - \frac{\theta_-}{2\eta}, \tag{43}$$

$$m_2 = \frac{1}{R} + \frac{1}{2\eta}\frac{1}{1/\theta_- + 1/\theta_+}, \tag{44}$$

$$m_3 = \frac{1}{R} - \frac{1}{2\eta}\frac{1}{1/\theta_- + 1/\theta_+ + 1/\theta_-}, \tag{45}$$

$$\tag{46}$$

with an obvious continuation of this sequence.

To see why this is the case consider the motion of points on a strange attractor. This will typically include points which impact the ramp repeatedly such that the values of $i_f$ and $v_f$ at the top of the ramp are evenly distributed about the origin. Now consider the point $\tilde{z} = \Sigma_{glob}(0,0)$. If $E$ and $R$ differ form $E_s$ and $R_s$ then this point will typically not be at the bottom of the ramp (see fig. 30). Starting at $\tilde{z}$ a

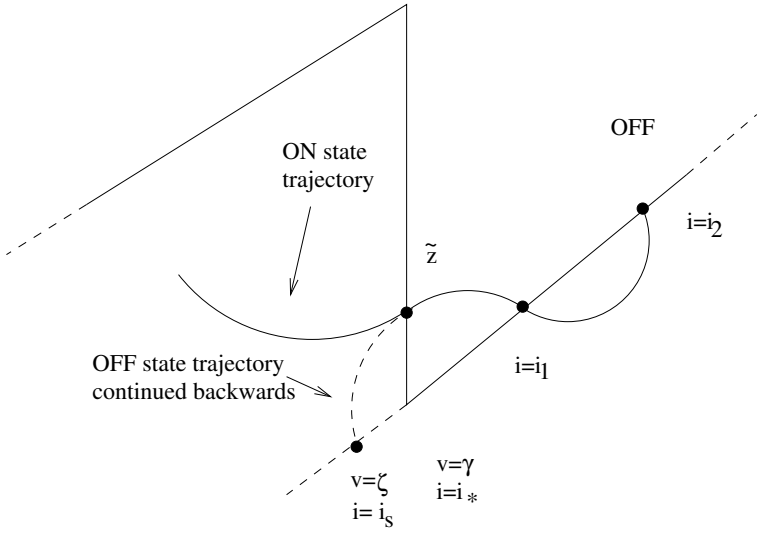


**Figure 30.** Location of the point at which $v = \zeta$ and subsequent intersections along the ramp

trajectory in (say) the OFF state intersects at a later point. If continued backwards $\tilde{z}$

will lie on an OFF state trajectory which would have intersected the ramp at a voltage $\zeta$ different from $\gamma$, where the current of the sliding solution is $i = i_s$. Observe that as $\zeta \to \gamma$, $i \to i_s$ and $(E, R) \to (E_s, R_s)$. This point represents the mean point of $A$-switchings of trajectories on the strange attractor.

Consider now an average trajectory on the attractor that $A$-switches at $v = \zeta$ with current $i_s + \delta$. The first switch on the ramp is then at a later time $2\delta/\theta_-$ at voltage

$$v = \zeta + \frac{2\delta\eta}{\theta_-},$$

with current

$$i_1 = \frac{2\delta\eta}{\theta_- R} - \delta + i_s.$$

We see that eliminating $\delta$ we have

$$i_1 = \left(\frac{1}{R} - \frac{\theta_-}{2\eta}\right)(v - \zeta) + i_s$$

This gives the equation of the first finger . The next switch is at

$$v = \zeta + \frac{2\delta\eta}{\theta_-} + \frac{2\delta\eta}{\theta_+}$$

with current

$$i_2 = \frac{2\delta\eta}{\theta_- R} + \frac{2\delta\eta}{\theta_+ R} + \delta + i_s$$

so that

$$i_2 = \left(\frac{1}{R} + \frac{1}{2\eta}\frac{1}{1/\theta_- + 1/\theta_+}\right)(v - \zeta) + i_s$$

giving the equation of the second finger. This argument extends to all fingers. The fractal structure of the actual fingers is due to small chaotic variations in the actual point of switching about the mean.

For $E = 35.0V$ we have that $\zeta \approx 11.1$ and the above values agree closely with the calculated attractors.

## 7. Conclusions

Some analytical explanation of the nonlinear behaviour of the DC/DC buck converter has been outlined. The importance of discontinuous phenomena such as grazing and sliding has been explained and the existence of a double spiral bifurcation diagram motivated analytically. The fundamental nature of our analysis strongly suggests that these features are to be found in a much wider class of piecewise smooth system. The generalisation of these phenomena to other Power Electronics converters shall be addressed in future work. Also, systems of the form (2) with a smooth switching signal instead of the ramp considered should be studied in details. We conjecture that for such systems the internal grazing phenomenon will be replaced by standard saddle-node bifurcations. These and other issues are the subject of current research.

**Acknowledgements**

The authors would like to thank Dr. Gerard Olivar, Universitat Politecnica de Catalunya, for the reproduction of figs. 10, 11 and his kind help and advice. Also, MdB is grateful to Dr. Francesco Vasca, Facoltá di Ingegneria, Universita' di Salerno, sede di Benevento for the fruitful discussions on the DC/DC converter problem.

## References


[1] Chris Budd and Felix Dux. Chattering and related behaviour in impact oscillators. *Phil. Trans. Royal Society London A*, 347:365–389, 1994.

[2] K. Chakrabarty, G. Poddar, and S. Banerjee. Bifurcation behaviour of the buck converter. *IEEE Transactions on Power Electronics*, 11:439–447, 1996.

[3] J.H.B. Deane and D.C. Hamill. Analysis, simulation and experimental study of chaos in the buck converter. *IEEE Power Electronics Specialists Conference*, pages 491–498, 1990.

[4] J.H.B. Deane and D.C. Hamill. Instability, sub-harmonics, and chaos in power electronic systems. *IEEE Transactions on Power Electronics*, 5:260–268, 1990.

[5] M. di Bernardo, A.R. Champneys, F. Garofalo, L. Glielmo, and F. Vasca. Nonlinear phenomena in closed loop dc/dc buck converter. *Proceedings NDES96 (Nonlinear Dynamics in Electronic Systems*, 1:51–56, 1996.

[6] M. di Bernardo, E. Fossas, G. Olivar, and F. Vasca. Secondary bifurcations and high periodic orbits in voltage controlled buck converter. *International Journal of Bifurcations and Chaos (to appear)*, 1997.

[7] M. di Bernardo, F. Garofalo, L. Glielmo, and F. Vasca. Quasi-periodic behaviours in dc/dc converters. *IEEE Power Electronics Specialist Conference*, 1996.

[8] M. di Bernardo, F. Garofalo, L. Glielmo, and F. Vasca. Switchings, bifurcations and chaos in dc/dc converters. IEEE Transactions on Circuits and Systems - I: Fundamental Theory and Applications (to appear), 1996.

[9] A.F. Filippov. *Differential Equations with Discontinuous Righthand Sides*. Kluwer Academic Press, 1988.

[10] S. Foale. Analytical determination of bifurcations in an impact oscillator. *Phil. Trans. Roy. Soc. London A*, 347:353–364, 1994.

[11] S. Foale and S.R. Bishop. Bifurcations in impact oscillators. *Nonlinear Dynamics*, 6:285–299, 1994.

[12] E. Fossas and G. Olivar. Study of chaos in the buck converter. *IEEE Transactions on Circuits and Systems - I: Fundamental Theory and Applications*, 43:13–25, 1996.

[13] P. Gaspard, R. Kapral, and G. Nicolis. Bifurcation phenomena near homoclinic systems: a two-parameter analysis. *J. Stat. Phys.*, 35:687–727, 1984.

[14] P. Glendinning and C. Sparrow. Local and global behavior near homoclinic orbits. *Journal of Statistical Physics*, 35:645–696, 1984.

[15] M.J.D. Powell. A hybrid method for nonlinear equations. In P. Rabinowitz, editor, *Numerical Methods for Nonlinear Algebraic Equations*. Gordon and Breach, 1970.

[16] C.K. Tse. Chaos from a buck switching regulator operating in discontinuous mode. *International Journal of Circuit Theory and Applications*, 22:263–278, 1994.

[17] C.K. Tse. Flip bifurcation and chaos in three-state boost switching regulators. *IEEE Transactions on Circuits and Systems - I: Fundamental Theory and Applications*, 41:16–23, 1994.

[18] C.K. Tse and W.C.Y. Chan. Instability and chaos in a current-mode controlled cuk converter. *IEEE Power Electronics Specialists Conference*, 1111-1117:608–613, 1995.

[19] D.M. Wolf, M. Verghese, and S.R. Sanders. Bifurcation of power electronic circuits. *Journal of the Franklin Institute*, 331B:957–999, 1996.

[20] G. Yuan, S. Banerjee, E Ott, and J.A. Yorke. Border-collision bifurcations in the buck converter. *IEEE Transactions on Circuits and Systems I (submitted to)*, 1997.

[21] I. Zafrany and S. Ben-Yakov. A chaos model of sub-harmonic oscillators in current mode pwm boost converters. *IEEE Power Electronics Specialists Conference*, 1996.